



**Target Chamber Issues for the Sandia  
National Laboratories Laboratory Microfusion  
Facility – Final Report for the Period 10/1/88  
through 12/31/90**

**R.R. Peterson, R.L. Engelstad, R.D. Griffin, H.Y.  
Khater, E.G. Lovell, J.J. MacFarlane, G.A. Moses, J.W.  
Powers, S.C. Rutledge, M.E. Sawan, P. Wang, O. Yasar**

**April 1991**

**UWFDM-854**

***FUSION TECHNOLOGY INSTITUTE  
UNIVERSITY OF WISCONSIN  
MADISON WISCONSIN***

### **DISCLAIMER**

This report was prepared as an account of work sponsored by an agency of the United States Government. Neither the United States Government, nor any agency thereof, nor any of their employees, makes any warranty, express or implied, or assumes any legal liability or responsibility for the accuracy, completeness, or usefulness of any information, apparatus, product, or process disclosed, or represents that its use would not infringe privately owned rights. Reference herein to any specific commercial product, process, or service by trade name, trademark, manufacturer, or otherwise, does not necessarily constitute or imply its endorsement, recommendation, or favoring by the United States Government or any agency thereof. The views and opinions of authors expressed herein do not necessarily state or reflect those of the United States Government or any agency thereof.

**Target Chamber Issues for the Sandia National Laboratories  
Laboratory Microfusion Facility—Final Report for the Period  
10/1/88 through 12/31/90**

R.R. Peterson, R.L. Engelstad, R.D. Griffin,\*  
H.Y. Khater, E.G. Lovell, J.J. MacFarlane,  
G.A. Moses, J.W. Powers,† S.C. Rutledge,  
M.E. Sawan, P. Wang, O. Yasar

Fusion Technology Institute  
Department of Nuclear Engineering and Engineering Physics  
University of Wisconsin-Madison  
Madison, WI 53706

April 1991

UWFDM-854

\*Present Address: Department of Materials Science, University of Alabama,  
Birmingham, AL 35294.

†Present Address: Naval Surface Warfare Center, Code H-13, Dahlgren, VA 22448

# Contents

<b>1. Introduction</b>	<b>1</b>
1.1. Scope of Work . . . . .	1
1.2. Publications and Presentations . . . . .	1
1.3. Target Chamber Designs . . . . .	5
<b>2. Blast Waves</b>	<b>7</b>
2.1. Target Emanations . . . . .	7
2.2. Vaporization by Target X-Rays . . . . .	7
2.3. First Surface Pressure Loading . . . . .	11
<b>3. Chamber Mechanical Response</b>	<b>15</b>
3.1. Pressure Loadings on the Chamber Wall . . . . .	15
3.2. Dynamic Response of the Chamber . . . . .	19
3.3. Chamber Lifetime Analysis . . . . .	25
<b>4. Target Support Structure</b>	<b>29</b>
4.1. Positioning . . . . .	29
4.2. Cryogenics . . . . .	30
<b>5. Post-Shot Operations</b>	<b>31</b>
5.1. Radioactivity . . . . .	31
5.2. Reentry . . . . .	35
5.3. Recovery and Refurbishing . . . . .	35
<b>6. Fragmentation</b>	<b>36</b>
<b>7. First Wall Material Experiments</b>	<b>39</b>
7.1. Experiments on SATURN . . . . .	40

7.1.1. Survival Experiments . . . . .	44
7.1.2. Shock Propagation Experiments . . . . .	44
7.2. Microstructural Analysis of SATURN Samples . . . . .	56
7.2.1. Sample Preparation . . . . .	57
7.2.2. Results . . . . .	58
<b>8. Fill Gas Heating by Ion Beams</b>	<b>64</b>
8.1. The SCATBALL Computer Code . . . . .	68
8.2. LMF Results . . . . .	69
<b>9. Conclusions</b>	<b>76</b>

## **1. Introduction**

### **1.1. Scope of Work**

This report attempts to summarize all work that the Fusion Technology Institute of the University of Wisconsin has performed on the Light Ion Laboratory Microfusion Facility (LMF) during the period from October 1, 1988 until December 31, 1990. A detailed discussion of work performed in the last year and three months of this period (October 1, 1989 through December 31, 1990) will be made. The work done in the earlier part of this period has already been presented in detail [?].

There were four tasks performed in this later period:

1. Analysis of the LMF target chamber.
2. Experiments on the response of first wall materials to intense x-rays.
3. Analysis of bulk structural response of the LMF target chamber.
4. Analysis of behavior of the fill gas in the LMF target chamber during heating by the driver ion beam.

There is some work not on the list of tasks that was done to assist in the writing of the Sandia contribution to the LMC Phase-II report. Also, there were changes in the priorities of the LMF effort at Sandia that affected our work. Therefore, the list of tasks is taken as a loose guide for our work. In this report, progress is discussed in these and other areas of LMF research.

### **1.2. Publications and Presentations**

Several reports and articles related to the LMF have been published:

1. J.J. MacFarlane, R.R. Peterson, and G.A. Moses, "Analysis of Physical Processes in ICF Target Chambers: Application to the Laboratory Microfusion Facility," University of Wisconsin Fusion Technology Institute Report UWFD-776 (October 1988) [also published in *Fusion Technology*, 15, 557 (March 1989)].

2. J.J. Ramirez, et al., "Design Issues for a Light Ion Beam LMF Driver," *Fusion Technology*, 15, 350 (March 1989).
3. R.R. Peterson, "Experiments to Simulate X-Ray Damage to the First Wall of the Inertial Confinement Fusion Laboratory Microfusion Facility," University of Wisconsin Fusion Technology Institute Report UWFD-806 (October 1989) [also published in the Proceedings of the 13th Symposium on Fusion Engineering, 2-6 October 1989, Knoxville, Tennessee].
4. H.Y. Khater and M.E. Sawan, "Dose Rate Calculations for a Light Ion Beam Fusion Laboratory Microfusion Facility," University of Wisconsin Fusion Technology Institute Report UWFD-809 (October 1989) [also published in the Proceedings of the 13th Symposium on Fusion Engineering, 2-6 October 1989, Knoxville, Tennessee].
5. R.R. Peterson, "Investigations into X-Ray Damage to the First Wall of the Inertial Confinement Fusion Laboratory Microfusion Facility," University of Wisconsin Fusion Technology Institute Report UWFD-816 (October 1989) [also to appear in *Laser Interaction and Related Plasma Phenomena, Volume 9* (Plenum Press, 1991), edited by H. Hora and G.H. Miley].
6. R.R. Peterson, "X-Ray Effects on First Surfaces in the Inertial Confinement Fusion Laboratory Microfusion Facility," University of Wisconsin Fusion Technology Institute Report UWFD-818 (December 1989).
7. R.R. Peterson, et al., "An Overview of Target Chamber Design and Analysis for the Light Ion Beam Laboratory Microfusion Facility," University of Wisconsin Fusion Technology Institute Report UWFD-819 (February 1990).

8. O. Yasar, "A Computational Model for Z-Pinch Plasma Channels," (PhD. thesis), University of Wisconsin Fusion Technology Institute Report UWFDM-823 (February 1990).
9. R.L. Engelstad, J.W. Powers, and E.G. Lovell, "Mechanical Design for the LMF Target Chamber," University of Wisconsin Fusion Technology Institute Report UWFDM-828 (October 1990) [also published in *Fusion Technology*, 19, 697 (1991)].
10. K.R. Prestwich, et al., "Design of a Light Ion Beam Driver for the Laboratory Microfusion Facility," Proceedings of BEAMS-90, July 1990, Novosibirsk, USSR.
11. R.R. Peterson, "Pressure Loadings on the Walls of a Light Ion Laboratory Microfusion Facility," University of Wisconsin Fusion Technology Institute Report UWFDM-833 (October 1990) [also published in *Fusion Technology*, 19, 686 (1991)].
12. J.J. Ramirez, et al., "A Light Ion Beam Driver for the Laboratory Microfusion Facility," *Fusion Technology*, 19, 664 (1991).
13. O. Yasar and G.A. Moses, "R-MHD: An Adaptive-Grid Radiation-Magnetohydrodynamics Computer Code," University of Wisconsin Fusion Technology Institute Report UWFDM-845 (January 1991).
14. J.W. Powers, "Structural and Fatigue Analysis of the Sandia Laboratory Microfusion Reactor Chamber," (M.S. thesis).
15. G.A. Moses, R.R. Peterson, and J.J. MacFarlane, "Analysis and Experiments in Support of ICF Reactor Concepts," to be published in *Physics of Fluids*.

Several presentations related to the LMF have been made at conferences. In some of these presentations, Sandia scientists were co-authors.

1. J.J. MacFarlane, R.R. Peterson, and G.A. Moses, "Analysis of Physical Processes in ICF Target Chambers: Application to the Laboratory Microfusion Facility," 8th Topical Meeting on the Technology of Fusion Energy, 3-9 October 1988, Salt Lake City, Utah.
2. J.J. Ramirez, et al., "Design Issues for a Light Ion Beam LMF Driver," 8th Topical Meeting on the Technology of Fusion Energy, 3-9 October 1988, Salt Lake City, Utah.
3. R.R. Peterson, "Experiments to Simulate X-Ray Damage to the First Wall of the Inertial Confinement Fusion Laboratory Microfusion Facility," 13th Symposium on Fusion Engineering, 2-6 October 1989, Knoxville, Tennessee.
4. H.Y. Khater and M.E. Sawan, "Dose Rate Calculations for a Light Ion Beam Fusion Laboratory Microfusion Facility," 13th Symposium on Fusion Engineering, 2-6 October 1989, Knoxville, Tennessee.
5. R.R. Peterson, "Investigations into X-Ray Damage to the First Wall of the Inertial Confinement Fusion Laboratory Microfusion Facility," 9th International Workshop on Laser Interaction and Related Plasma Phenomena, 6-10 November 1989, Monterey, California.
6. K.R. Prestwich, et al., "Design of a Light Ion Beam Driver for the Laboratory Microfusion Facility," BEAMS-90, July 1990, Novosibirsk, USSR.
7. R.L. Engelstad, J.W. Powers, and E.G. Lovell, "Mechanical Design for the LMF Target Chamber," 9th Topical Meeting on the Technology of Fusion Energy, 7-11 October 1990, Oak Brook, Illinois.
8. R.R. Peterson, "Pressure Loadings on the Walls of a Light Ion Laboratory Microfusion Facility," 9th Topical Meeting on the Technology of Fusion Energy, 7-11 October 1990, Oak Brook, Illinois.

9. J.J. Ramirez, et al., “A Light Ion Beam Driver for the Laboratory Microfusion Facility,” 9th Topical Meeting on the Technology of Fusion Energy, 7-11 October 1990, Oak Brook, Illinois.
10. G.A. Moses, R.R. Peterson, and J.J. MacFarlane, “Analysis and Experiments in Support of ICF Reactor Concepts,” Annual Meeting of the American Physical Society Division of Plasma Physics, November 7-11, 1990, Cincinnati, OH.
11. R.R. Peterson, “Plasma Conditions in Light Ion Beam Heated Target Chamber Fill Gases,” Annual Meeting of the American Physical Society Division of Plasma Physics, November 7-11, 1990, Cincinnati, OH.
12. P. Wang, J.J. MacFarlane, and G.A. Moses, “Analysis of  $K\alpha$  X-Ray Satellites from a Target Heated by an Intense Ion Beam,” Annual Meeting of the American Physical Society Division of Plasma Physics, November 7-11, 1990, Cincinnati, OH.

### **1.3. Target Chamber Designs**

Two target chamber designs are under consideration for the light ion LMF: one where the minimum distance between the target and the chamber wall is 150 cm and the other where this distance is 300 cm. The two designs are pictured in Fig. 1.1. They are both essentially cylindrical designs with end volumes for experimental space. Both designs use a first wall liner made of 4-directionally woven graphite to mitigate the effects of rapid vaporization on the supporting structures. In both designs the ion beams are propagated to the target through 1 torr helium gas 150 cm from lens magnets. In the 150 cm radius design the lenses are therefore positioned near the first wall. In the 300 cm radius design, the lens magnets protrude into the target chamber. For simplicity, the lens magnets are not shown in Fig. 1.1. The large radius design is thought to have better conditions for some of the simulation experiments. It is also easier to design a wall to withstand the target explosion for the large chamber because of the lower x-ray fluence, although the design of

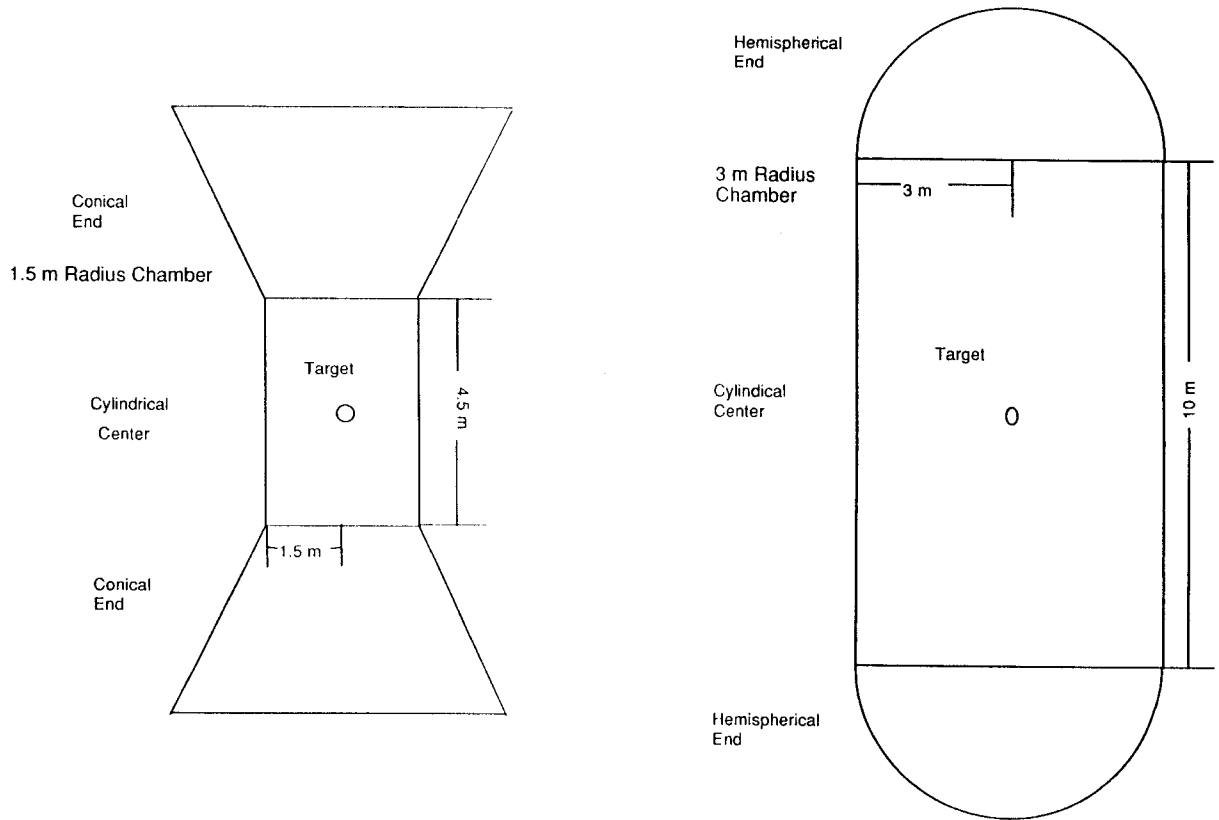


Figure 1.1. Two target chamber designs for the light ion LMF.

a wall for the smaller chamber has also been achieved. The large design has a significantly larger volume, which reduces the residual pressure in the chamber that is present for a long period after the target explosion. Both designs have shielding in the form of a Boral liner on the outside surface of the chamber wall and a borated water filled tank surrounding the entire chamber.

## **2. Blast Waves**

### **2.1. Target Emanations**

It was assumed that the target emanations are those that would be released from the ion beam target design that was published several years ago by LLNL [?]. This target design is shown in Fig. 2.1. It has been calculated [?] that this target emits 68% of its yield in neutrons, 20% in x-rays and 10% in debris ions. The remaining 2% is lost in endoergic nuclear reactions. A time-integrated x-ray spectrum is shown in Fig. 2.2 in arbitrary units. This x-ray energy is released in a pulse roughly 1 ns long, as is shown in Fig. 2.3. Here the total x-ray power from the target is shown, in arbitrary units, plotted against time. The structure in Fig. 2.3 is due to different physical processes occurring during the target burn. The target debris are taken to be 260 keV lead ions. The target yield in this work ranges between 0 and 1000 MJ. The shapes of the ion and x-ray spectra and the energy partitioning are assumed to be independent of the target yield. To obtain the target emanations for a given yield, Figs. 2.2 and 2.3 are scaled to the proper total energy.

### **2.2. Vaporization by Target X-Rays**

The target x-rays reach the surface of the woven graphite wall liner 5 or 10 ns after the target microexplosion. The x-ray fluence is potentially high enough to vaporize a layer of graphite. This has been analyzed with the CONRAD [?] computer code and provides the calculated thickness of the vaporized layer for various combinations of target yield and target chamber wall radius. A target yield of 1000 MJ and a wall radius of 150 cm leads to an x-ray fluence of 707 J/cm<sup>2</sup> and a vaporized thickness of 17  $\mu$ m. The shielding effect of

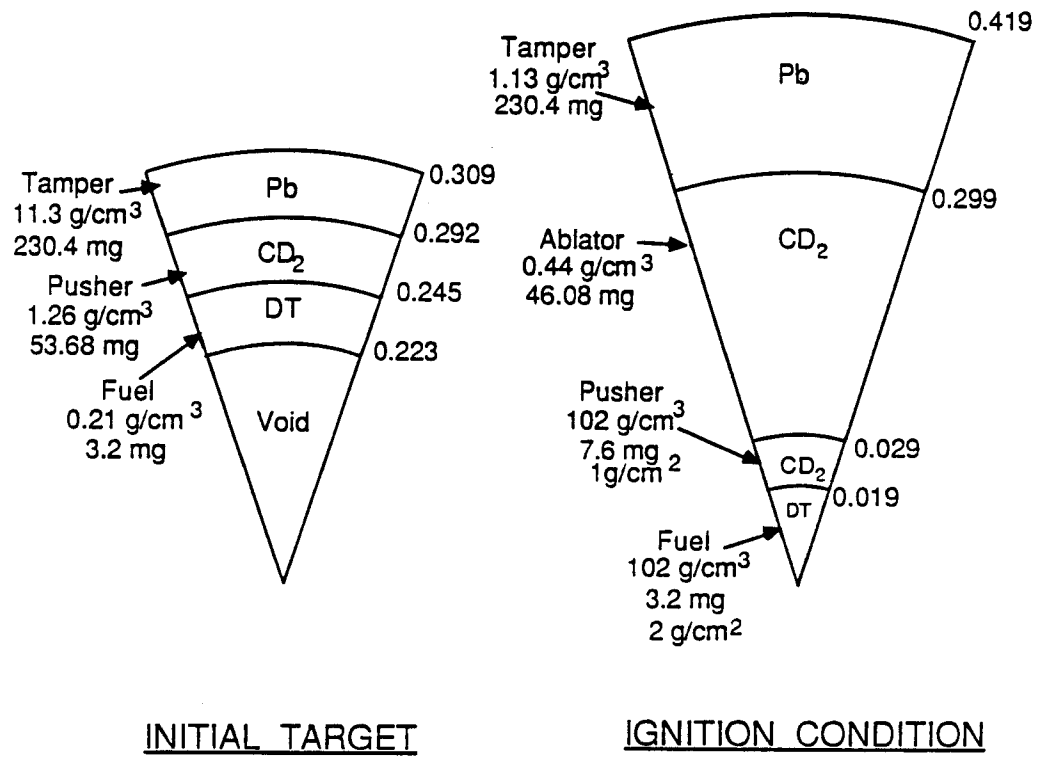


Figure 2.1. Ion beam target design.

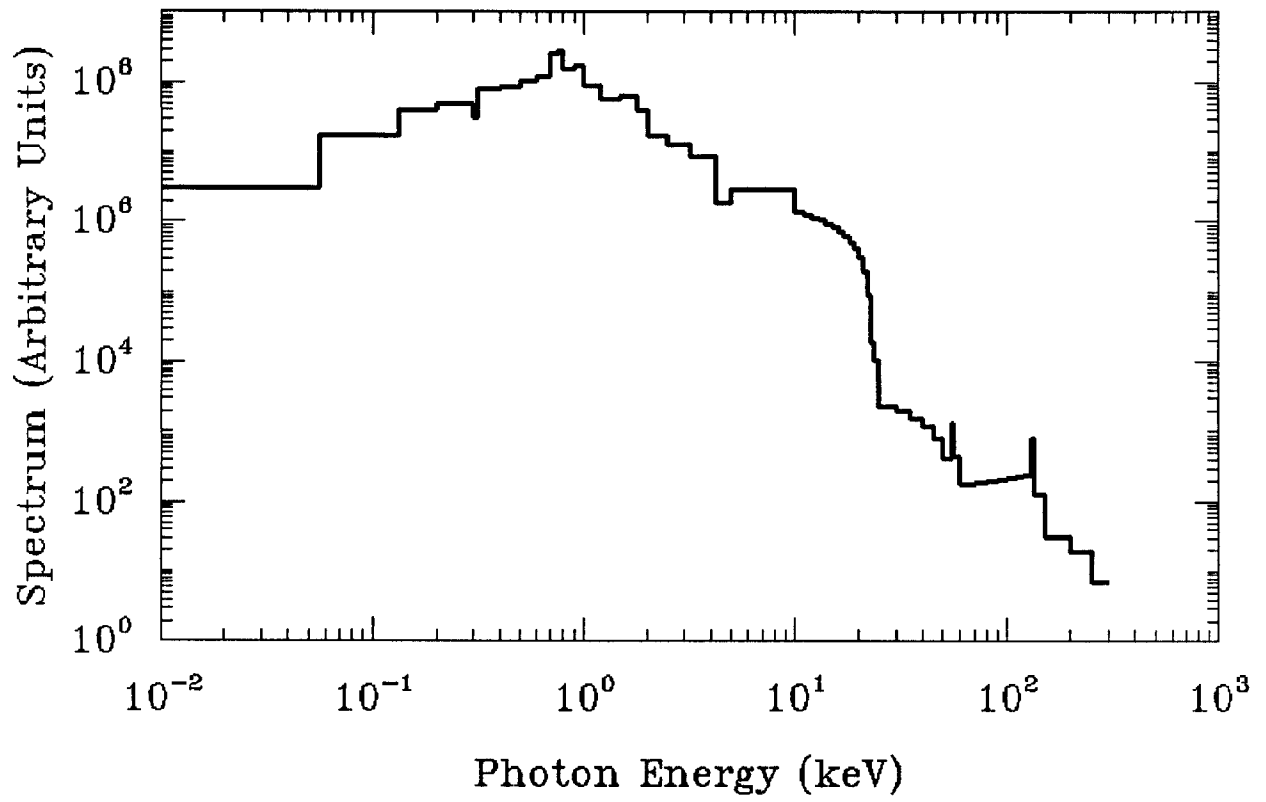


Figure 2.2. Time-integrated x-ray spectrum from the LIBRA target.

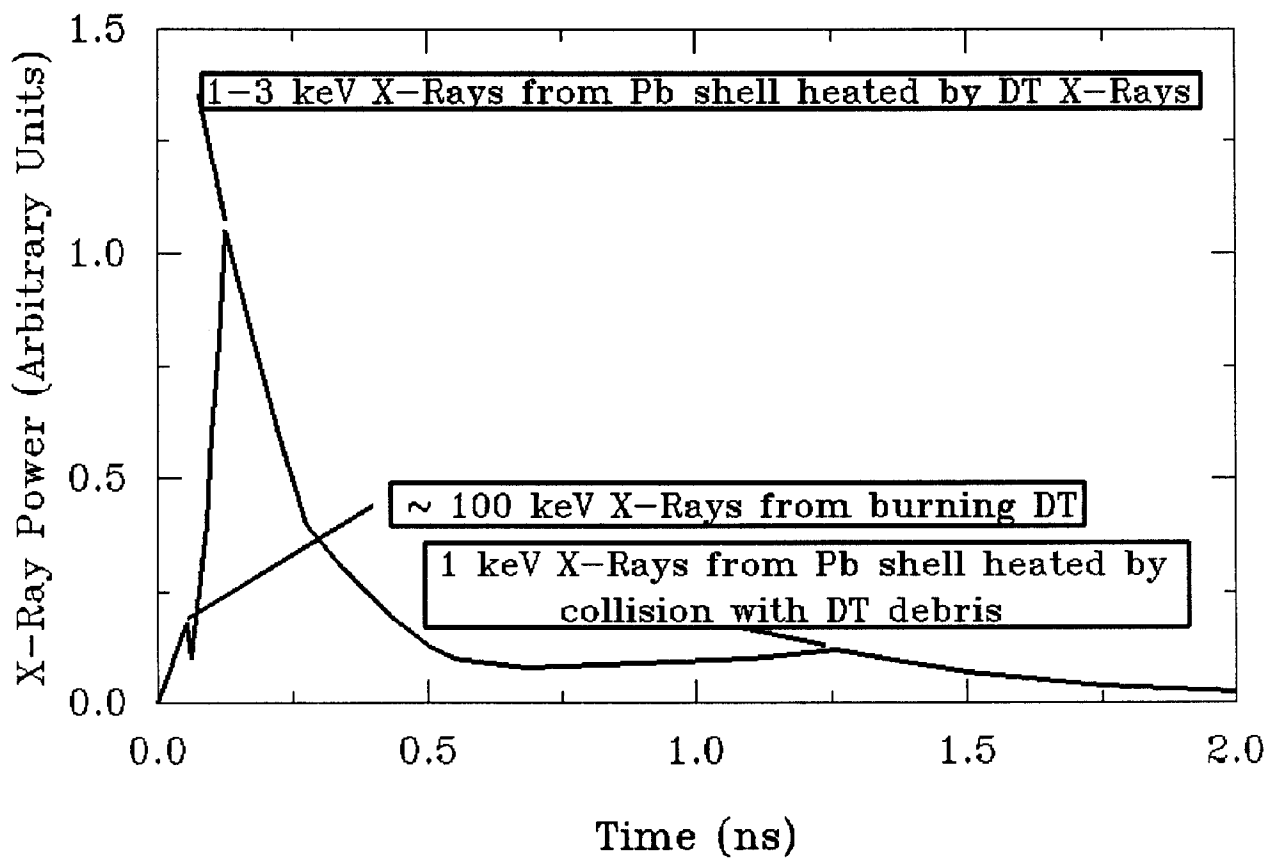


Figure 2.3. X-ray power from LIBRA target versus time.

1 torr of helium is not important. A shock is formed in the vapor layer that propagates to the wall over a time long compared with the x-ray pulse width. The vapor moves into the target chamber and intersects the debris ions 10's of cm from the wall. The ion energy can only contribute to vaporization indirectly, by heating the vapor and causing it to radiate back to the wall over roughly a  $\mu\text{s}$  time scale. The results, pictured in Fig. 2.4, show how the thickness varies with the x-ray fluence.

The long term behavior of the vapor is complex and difficult to calculate. Rapid decompression of the vapor cools the vapor, perhaps to the point where homogeneous condensation on nucleation sites can occur forming droplets that move throughout the chamber until they strike a surface. If heating of the vapor by the debris ions can prevent droplet formation, the vapor will eventually condense on some surface.

### **2.3. First Surface Pressure Loading**

The pressure loading on the target chamber walls of the light ion LMF consists of two components which have been termed the vaporization and residual pressures [?]. The vaporization pressure results from the shock that passes through the vaporized graphite and strikes the unvaporized portion of the wall. The vaporization pressure occurs some time after the x-ray pulse has ceased and is characterized by a duration which is typically 1 ns. The timing and width of the vaporization pressure pulse is a function of the width of the vaporized layer. The shock is formed by the deposition of x-rays in the vapor, which causes steep temperature and pressure gradients in the vapor. This shock propagates through the vapor to the remaining solid part of the wall, imposing a large mechanical pressure on the wall. This shock propagation is shown for a 1000 MJ yield target and a 300 cm radius chamber in Fig. 2.5, where the pressure is represented by various shades of gray, over a position versus time plane. The pressure at the vapor/solid interface as a function of time is shown in Fig. 2.6. The residual pressure is a long term pressure due to energy that is carried into the chamber volume with the vaporized graphite. The residual pressure

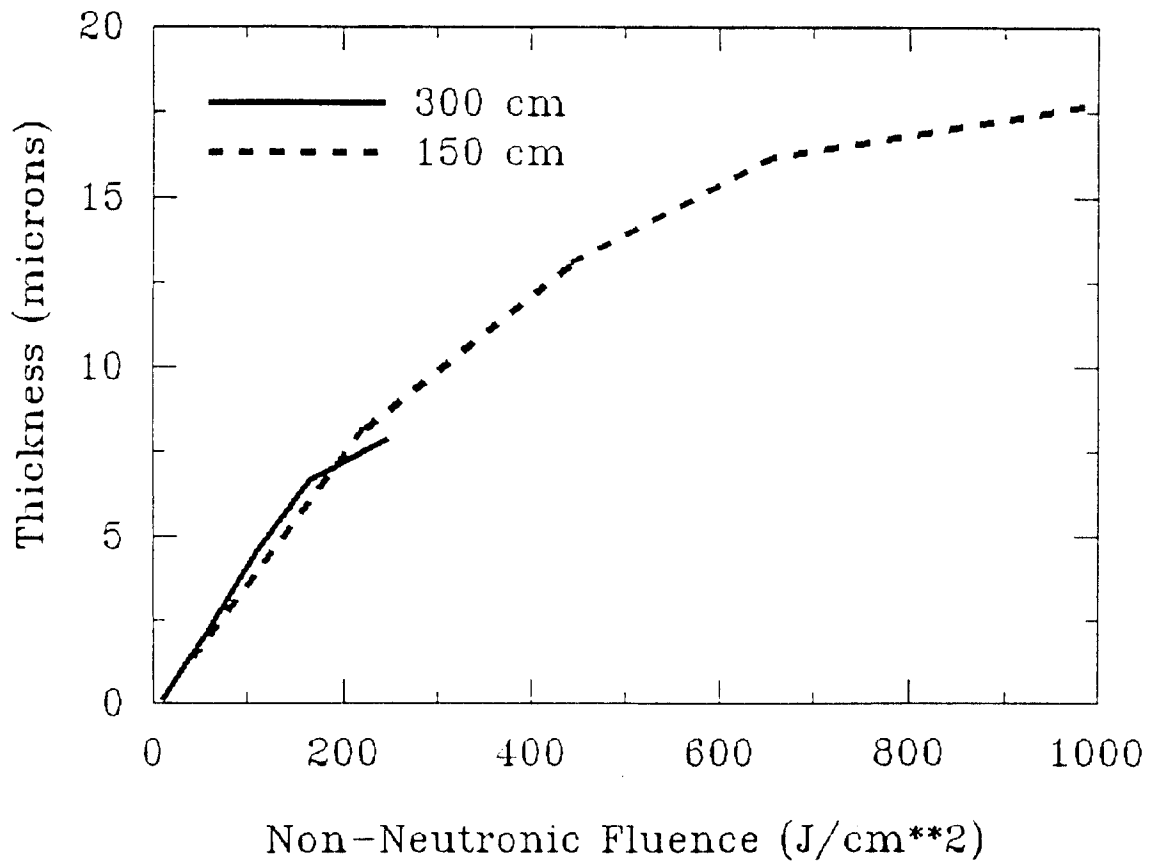


Figure 2.4. Thickness of vaporized graphite layer versus x-ray fluence.

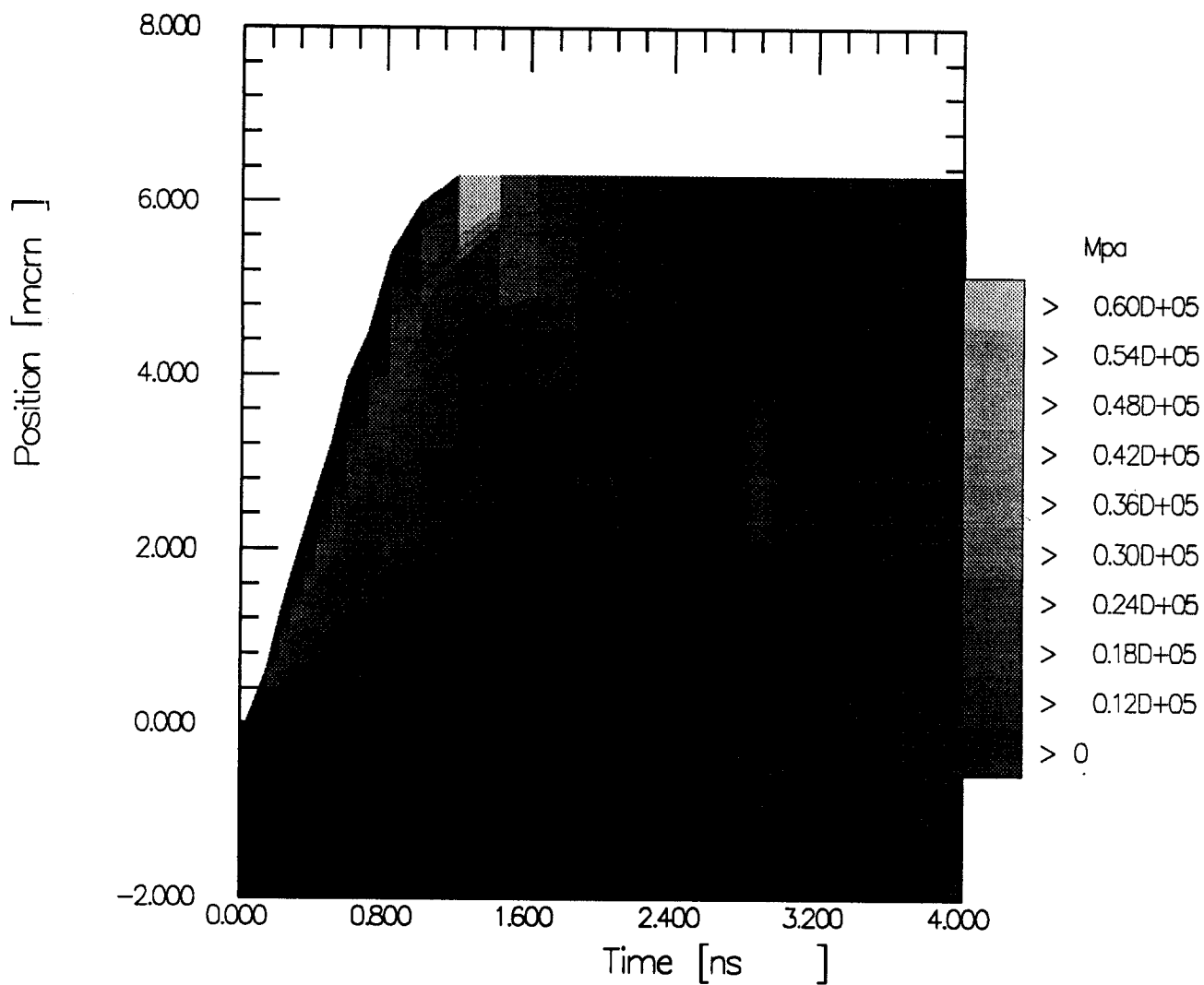


Figure 2.5. Pressure plotted over position versus time plane. The target yield is 1000 MJ, the wall radius is 300 cm, and the wall material is graphite.

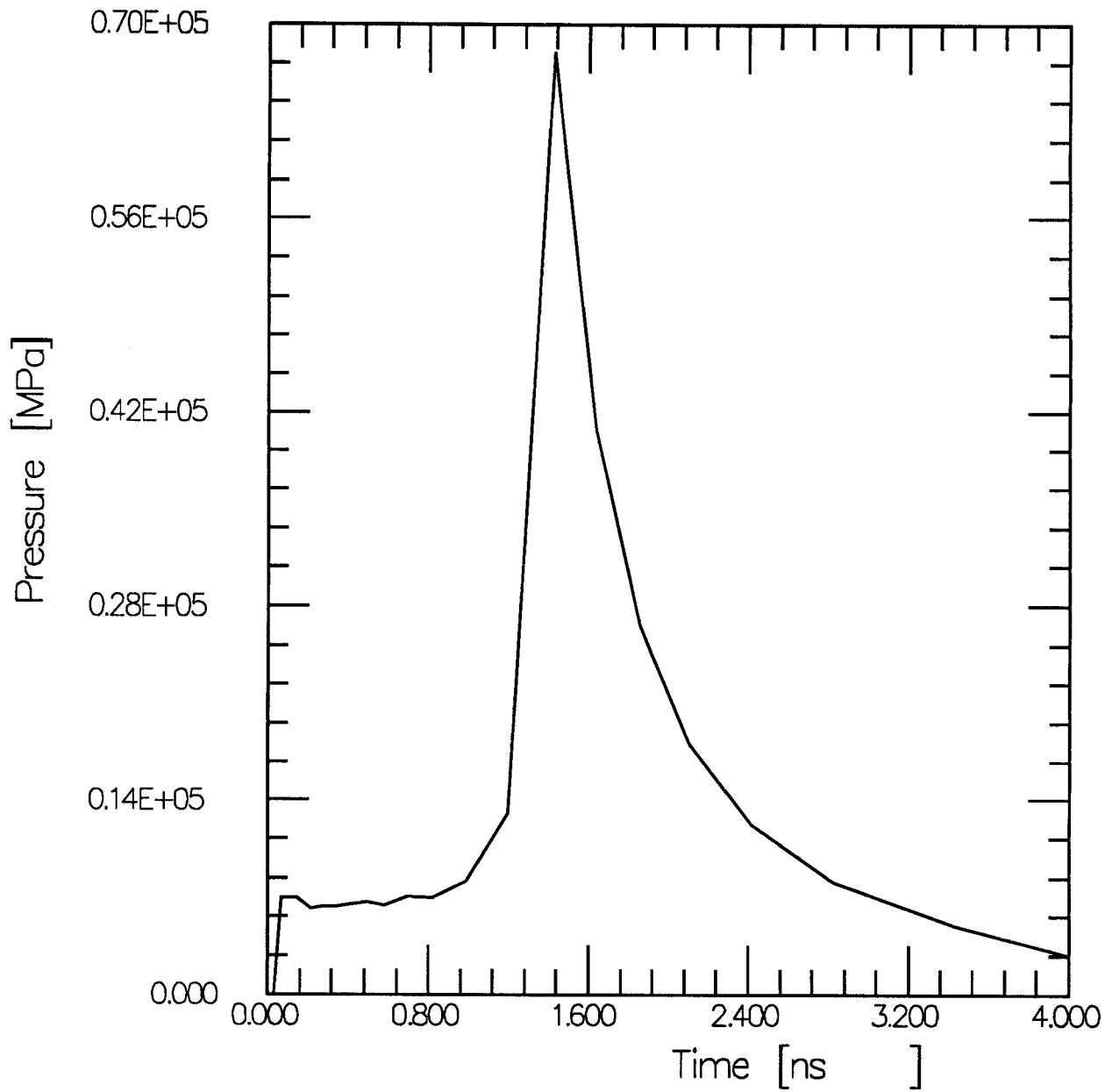


Figure 2.6. Pressure at the vapor/solid interface versus time. The target yield is 1000 MJ, the wall radius is 300 cm, and the wall material is graphite.

is estimated to be  $(\gamma - 1) E/V$ , where  $\gamma$  is the ratio of specific heats,  $E$  is the energy in the chamber as determined by CONRAD simulations, and  $V$  is the volume of the target chamber. The CONRAD simulations indicate that  $\gamma$  is typically 1.5 for these chamber designs.

The peak vaporization pressure is plotted against x-ray fluence in Fig. 2.7. The peak pressure for a 150 cm radius target chamber and a 1000 MJ yield is roughly 150 GPa. For a 300 cm radius chamber, the peak pressure is 75 GPa. In both cases the pressure is far beyond the strength of the solid material, so shocks will be launched into the material. To mitigate the effects of this shock, 4-directional woven graphite was chosen as a first wall liner. The material is nonhomogeneous and it is hoped that the shock strength will be rapidly attenuated due to reflections at the edges of fibers in the graphite composite. The survivability of different forms of graphite under pulsed x-ray irradiation are currently being tested on the SATURN facility at Sandia National Laboratories. A sample of 4-directional woven graphite has been subjected to 4 pulses of 1-3 keV x-rays at a fluence per pulse of 220 J/cm<sup>2</sup> without any noticeable damage [?]. This is more than the fluence from a 1000 MJ target explosion on a 300 cm radius. The pressure in the SATURN experiments at the vapor/solid interface has been calculated to be 18 GPa. The pressure impulse on the LMF target chamber wall, integrated in time out to a point well past the end of the vaporization pressure pulse, is shown in Fig. 2.8 plotted against x-ray fluence. This, along with the residual pressure, shown in Fig. 2.9, allows for analysis of the mechanical response of the target chamber wall.

### **3. Chamber Mechanical Response**

#### **3.1. Pressure Loadings on the Chamber Wall**

As described in Section 1.3, two target chamber designs have been analyzed for LMF, i.e., cylindrical chambers having radii of 1.5 m and 3.0 m. Both designs are 4.5 m in height

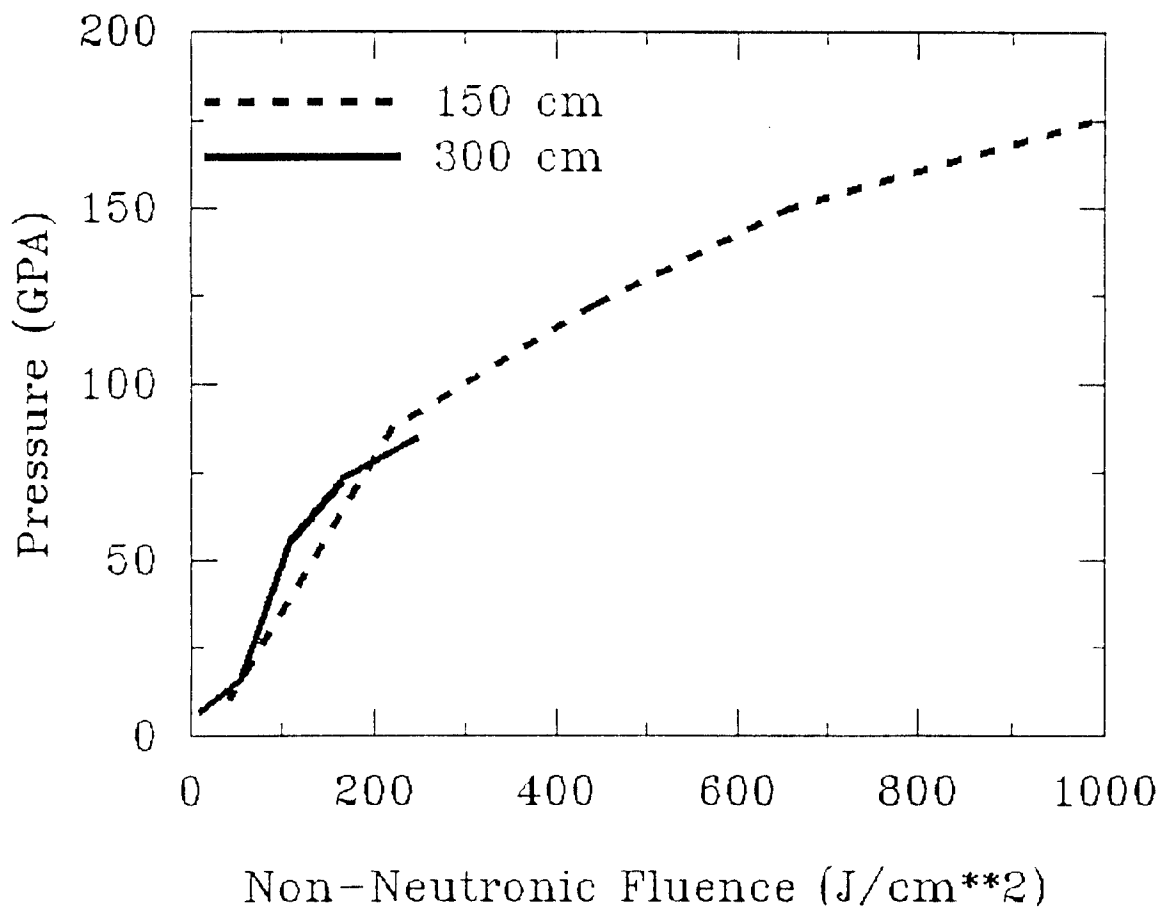


Figure 2.7. Peak vaporization pressure at the vapor/solid interface of the light ion LMF.

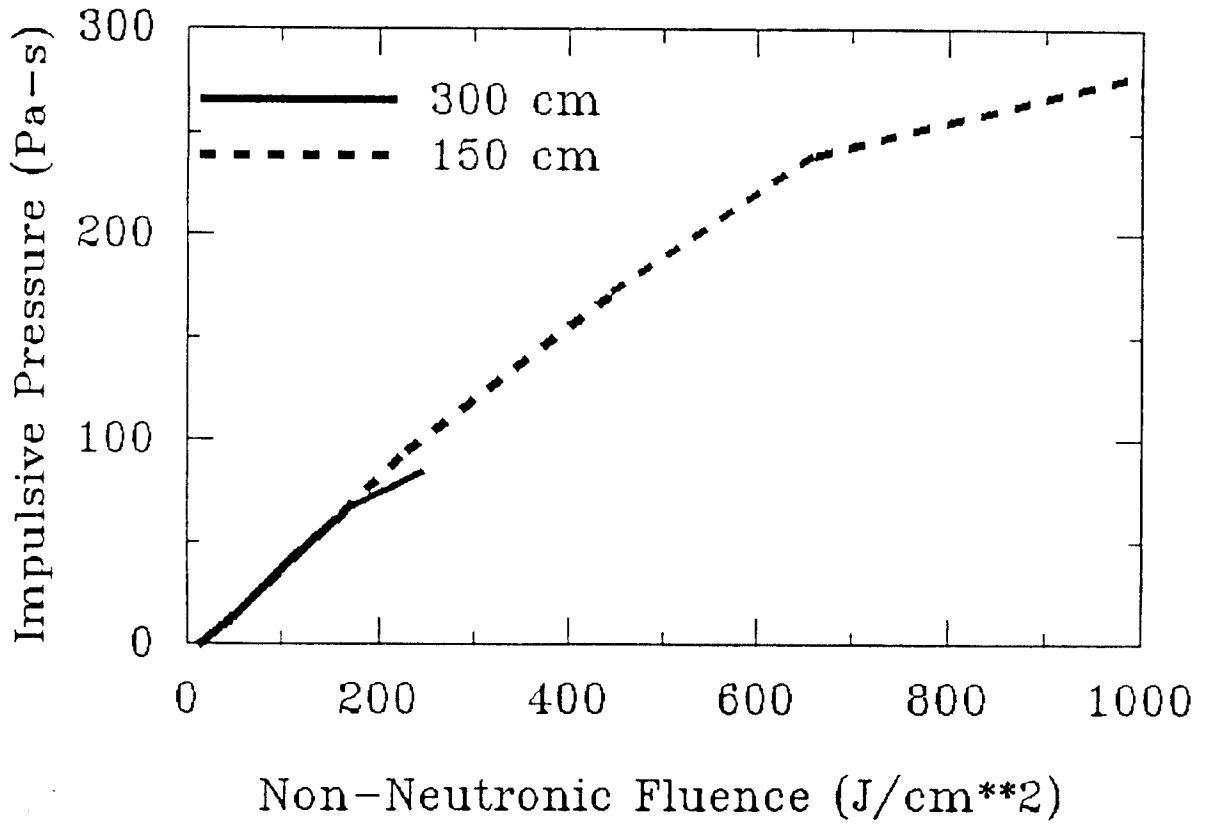


Figure 2.8. Pressure impulse at the vapor/solid interface of the light ion LMF.

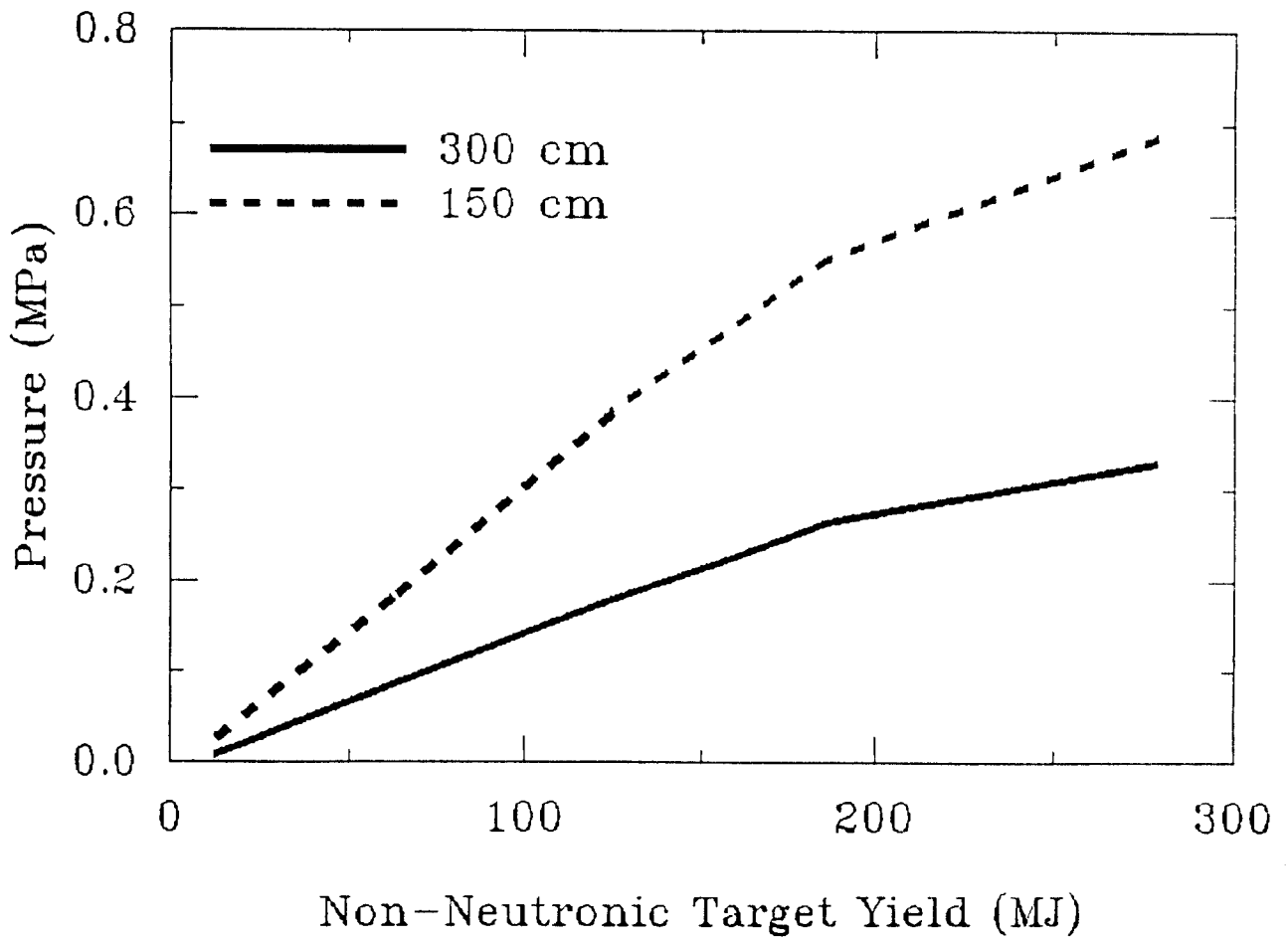


Figure 2.9. Residual pressure in LMF target chamber versus non-neutronic yield.

with 3 circumferential rows of beam ports having 12 ports per row. The ports are 36 cm in diameter and are arranged to form either triangular or square perforation patterns.

In Section 2.3, the two components of the pressure loading were described as being either a short duration impulse or a long duration afterpressure. For example, Fig. 2.6 shows a pressure history for a 1000 MJ target yield where the duration of the initial spike is on the order of a few nanoseconds. Thus, when compared with the response time of either shell (i.e., the natural period of vibration), the loading can be characterized as an impulse. In addition to this initial impulse, a steady afterpressure of a sizable amount follows. Table 3.1 shows the pressure loadings considered in this analysis for various target yields at the two different radii. The residual pressures, referred to as  $P_{static}$ , were computed from  $(\gamma - 1)E/V$  as discussed in Section 2.3.

The actual shape of the pressure versus time curve after the initial spike has not been fully identified. A worst case model of the afterpressure would be a dynamic step function which is superimposed with the impulse load (see Fig 3.1). However, a more accurate representation of the afterpressure history would be a “ramped step” such as the model shown in Fig. 3.2. The CONRAD code has been used to predict the times  $t_2$  and  $t_3$ , which characterize this ramp loading. For example, for the chamber of radius 1.5 m,  $t_2$  is approximately 0.1 ms and  $t_3$  is 0.8 ms; for the chamber of radius 3.0 m,  $t_2$  is 1.07 ms and  $t_3$  is 1.32 ms.

### **3.2. Dynamic Response of the Chamber**

The pressure loads are assumed to be uniformly distributed over the first wall of the chamber, resulting in an axisymmetric mechanical response that is also symmetric with respect to the midspan plane. The target chamber is modeled as a thin-walled cylindrical shell with clamped boundary conditions at both ends. In addition, it is assumed to be restrained from expanding axially. The largest stresses in the cylinder will occur (due to bending) at the location of the rigid end supports. However, localized thickening of

Table 3.1. Pressure Loadings on the LMF Chamber.

**Case I: Radius = 1.5 m**

Target Yield (MJ)	Impulsive Pressure (Pa-s)	Residual Pressure $P_{static}$ (MPa)
1000	284	0.77
200	55	0.22
50	10	0.062
10	0.7	0.0062

**Case II: Radius = 3.0 m**

Target Yield (MJ)	Impulsive Pressure (Pa-s)	Residual Pressure $P_{static}$ (MPa)
1000	84.5	0.3310
200	14.9	0.0733
50	2.13	0.0145
10	0.11	0.0018

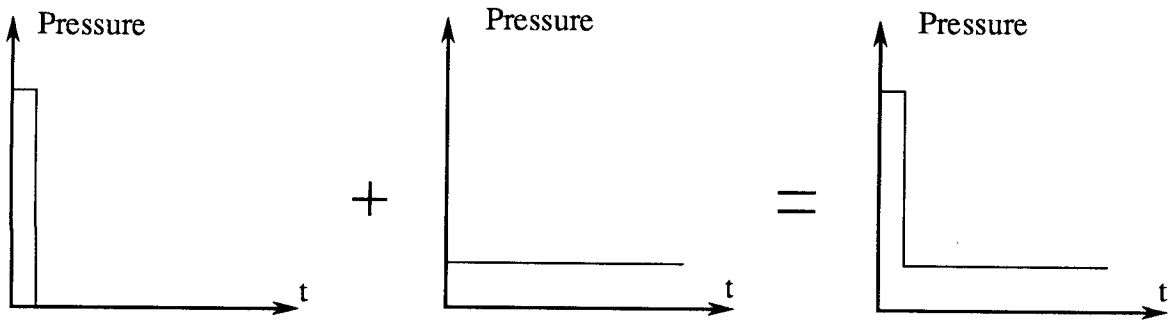


Figure 3.1. Typical impulse superimposed with a step load.

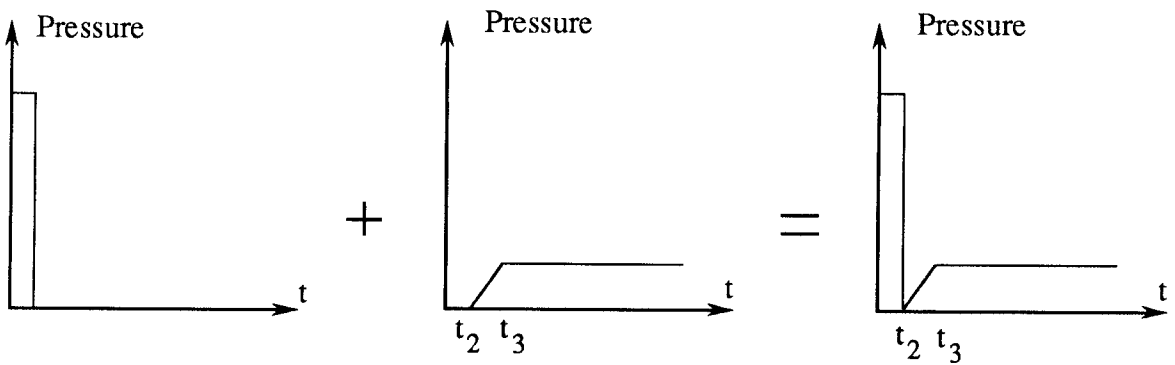


Figure 3.2. Typical impulse superimposed with a ramped step load.

the chamber walls in this region can control these stresses; therefore, the shell design is based on the minimum thickness needed at the midspan. It is also assumed that the longitudinal (or axial) stress is zero at the midspan, resulting in a uniaxial state of stress (in the circumferential direction) at this location.

To show the effects of the various types of pressure loadings described above, an unperforated steel chamber with a radius of 1.5 m and a thickness of 5.0 cm is used. Figure 3.3 shows the circumferential stress history at the midspan of the chamber caused by a single impulsive load of 284 Pa-s (corresponding to a 1000 MJ yield). From the plot it can be seen that the impulse causes the chamber to oscillate about the zero stress axis, producing maximum stresses around 30 MPa. The 2% damping assumed for the chamber causes these stresses to approach zero in a very short time. The circumferential stresses that result from a single step load with a magnitude of 0.77 MPa are shown in Fig 3.4. If allowed to damp completely, the final stress level will match that given by a 0.77 MPa static pressure. To determine the response of the chamber to the combined effects of impulsive and step loads, i.e., as in Fig. 3.1, the results from the two separate load cases are superimposed. The total stress history resulting from a 284 Pa-s pressure pulse and a 0.77 MPa afterpressure is shown in Fig. 3.5. The combined dynamic effects produce a rather severe response, driving the peak stress to over 60 MPa. However, it is assumed that the actual pressure loading is better characterized by an impulse with a ramped step (as in Fig. 3.2). Figure 3.6 shows the response of the same chamber using a 284 Pa-s impulse superimposed with a ramp that starts at 0.1 ms and reaches 0.77 MPa at 8 ms. Since the ramped step load is less severe than the step load, the magnitude of the oscillations is somewhat smaller. In addition, the response of the impulse alone is slightly out of phase from the response of the ramped step, causing a reduction in the total stress when the two are superimposed. It should be noted, however, that the phase shift depends on the ramp times  $t_2$  and  $t_3$  relative to the period of the shell.

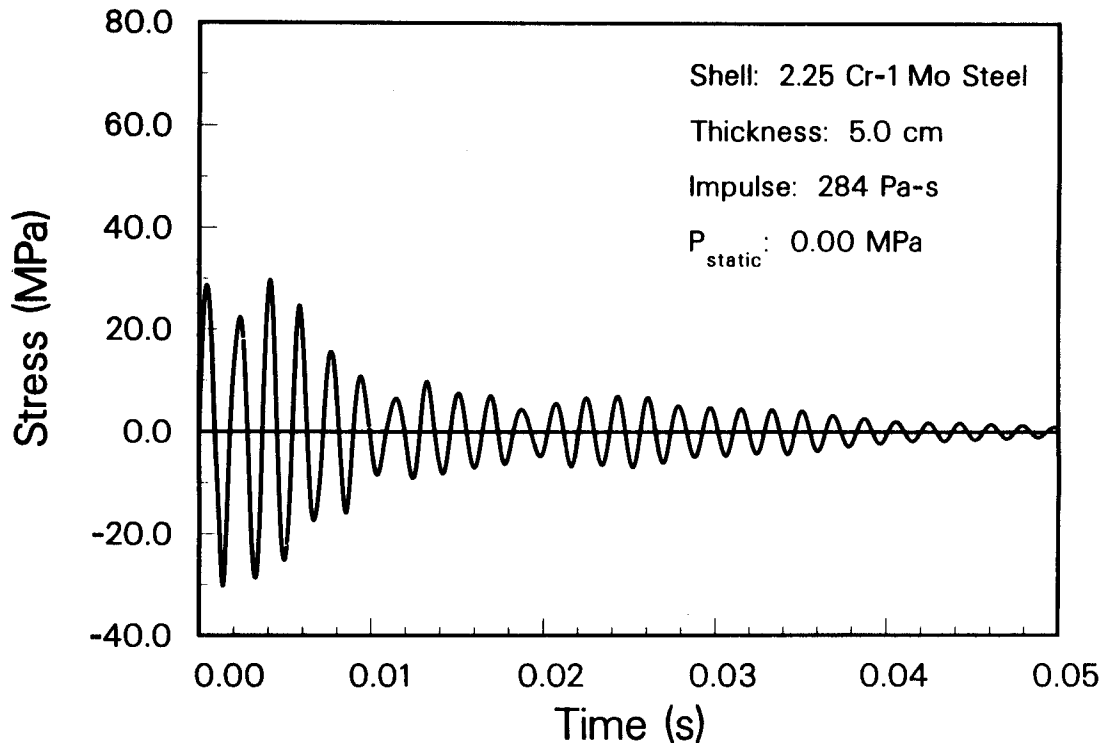


Figure 3.3. Circumferential stresses produced by an impulsive load.

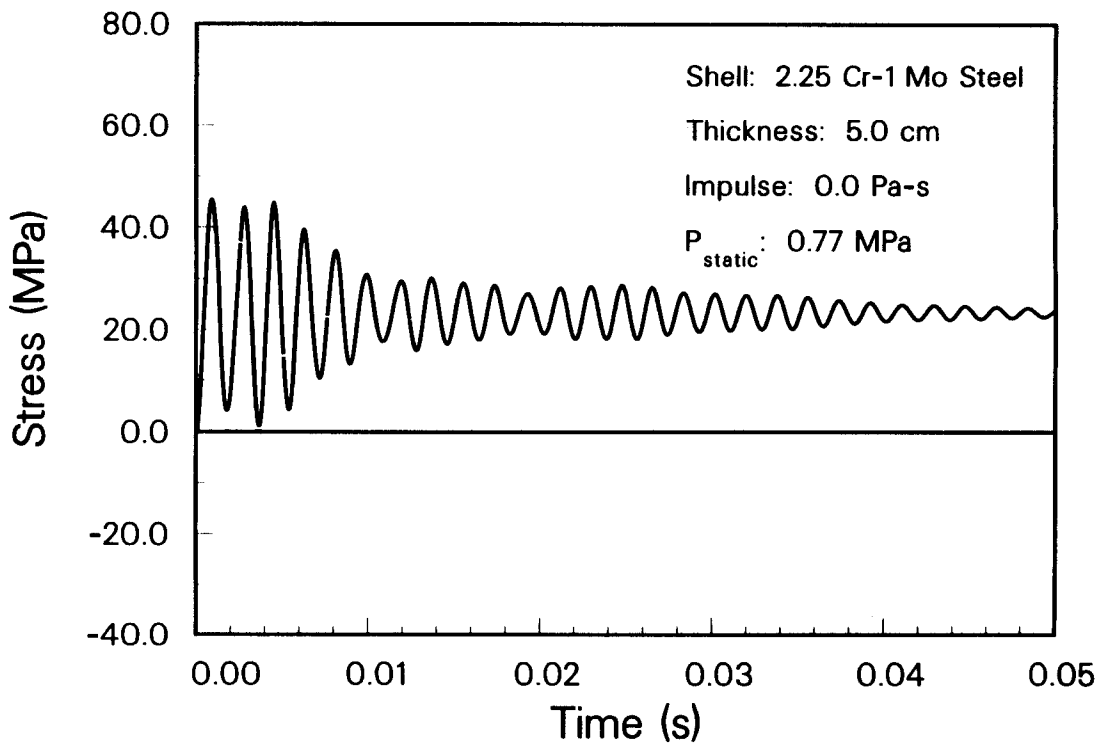


Figure 3.4. Circumferential stresses produced by a step load.

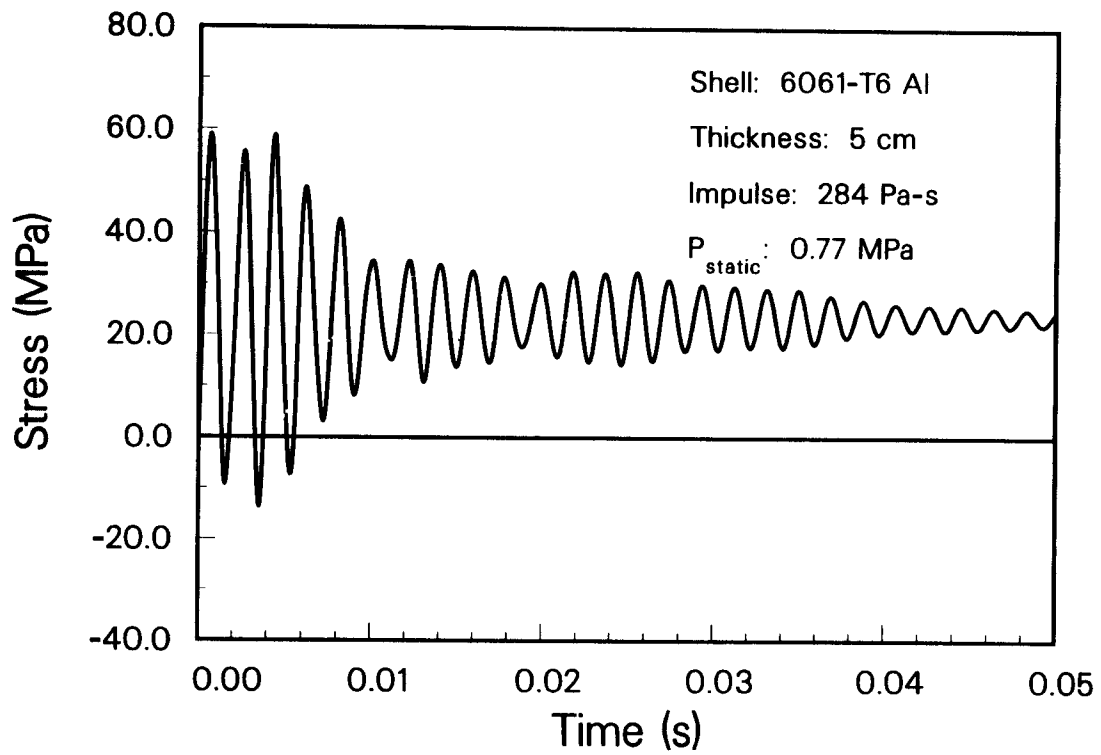


Figure 3.5. Circumferential stresses produced by an impulsive load superimposed with a step load.

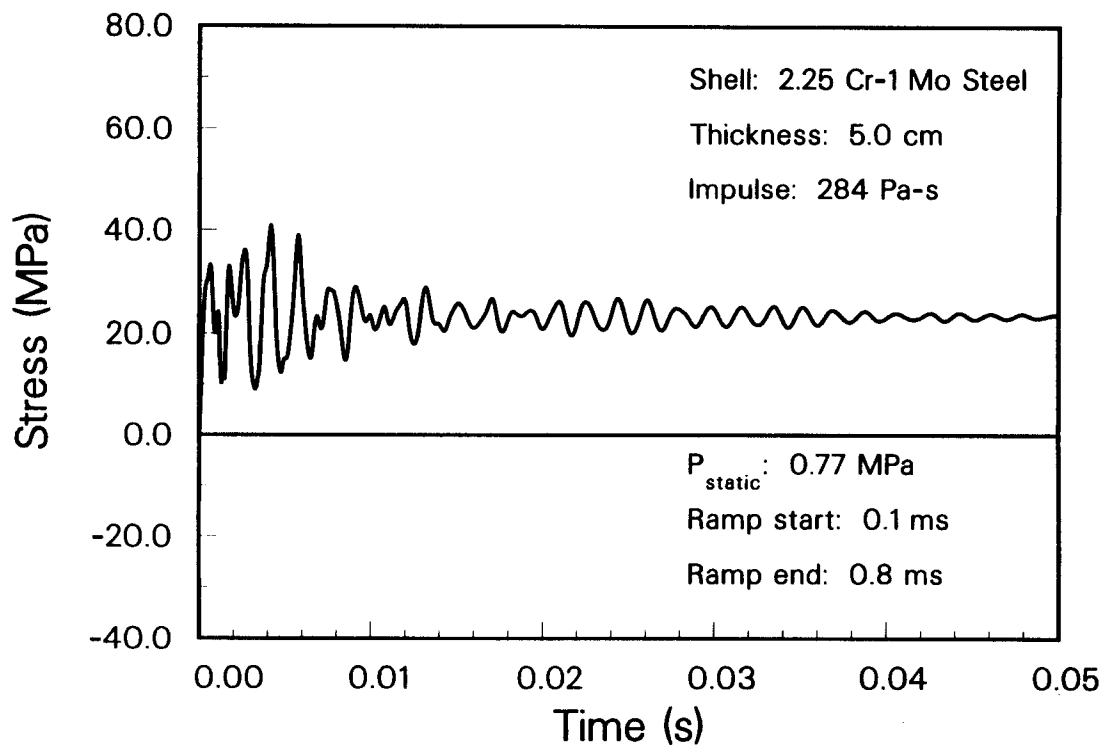


Figure 3.6. Circumferential stresses produced by an impulsive load superimposed with a ramped step load.

Comparing the dynamic response from each load type, the importance of including the afterpressure in all fatigue calculations is obvious. What may seem like a relatively insignificant residual pressure, may actually produce a substantial mean stress in addition to amplifying the alternating stress. The rise time of the ramp is also an important parameter affecting the magnitude and general characteristics of the response. If a means were devised of venting the afterpressure so that the rise time was increased and the peak static pressure was decreased, the actual strains and stresses developed in the chamber would be substantially reduced.

As previously noted, the response calculations presented above have been based upon the assumption that the shell was complete, i.e., unperforated. With the relatively large number of beam ports encircling the chamber, the mechanical response of the first wall will actually be characterized by more compliance. To account for this effect, modified elastic constants are used in place of actual material properties, e.g., Young's modulus and Poisson's ratio. This has been done for both triangular and square perforation patterns. Details of this procedure along with the equivalent material properties used in the calculations have been reported in UWFDM-819 [1].

### **3.3. Chamber Lifetime Analysis**

Cumulative damage is assessed in the fatigue analysis since each stress (or strain) history is characterized by cycles of different amplitude and each target yield will produce a different history. Because of the mean stresses (or strains) present in addition to the alternating stresses (or strains), a rainflow cycle counting method was used to determine an equivalent history that could be used with the constant amplitude, fully reversed fatigue data. A Goodman diagram was used in conjunction with the cycle counting in order to obtain the value of the equivalent range stress (or strain), then Miner's rule was applied to estimate the linear, cumulative damage effects. Two materials were considered in the structural analysis of the LMF chamber, 2.25 Cr-1 Mo steel and 6061-T6 aluminum (unwelded

Table 3.2. LMF Cumulative Shots.

Lifetime Years	Target Yield			
	10 MJ	50 MJ	200 MJ	1000 MJ
3	990	480	30	0
6	1800	1080	90	30
9	1950	2130	330	90
12	2010	2970	810	210
30	2190	5490	5850	1470

and welded). The actual fatigue data used for all calculations in addition to the details of the procedure used for the fatigue analysis can be found in UWFD-819 [1].

Fatigue calculations were carried out for lifetimes of 3, 6, 9, 12 and 30 years. Table 3.2 shows the cumulative shots for each of the target yields considered. The results of the fatigue calculations were governed by the loadings of the 1000 MJ shots for both the steel and the aluminum, the primary failure mode being yielding. Consequently, the value of the thickness remains the same for lifetimes of 6, 9, 12 and 30 years in each case. However, with no 1000 MJ shots present in the first 3 years, the value of the minimum thickness drops significantly. For example, Table 3.3 gives the chamber thicknesses needed for a 3 year lifetime, while Table 3.4 provides the results for the 6, 9, 12 and 30 year lifetimes. The effect of using the ramped step load model is also reflected in the required values of the thicknesses, i.e., substantial reductions can be seen. It should be noted that a number of the fatigue calculations show the chamber can be built with relatively thin walls depending on the material, lifetime, etc. Since buckling becomes an issue for such cases, a 3 cm lower limit is recommended for the chamber thickness.

Table 3.3. Minimum Thicknesses Needed for a Lifetime of 3 Years.

**Case I: Radius = 1.5 m**

Material	Port Pattern	Minimum Thickness (cm)	
		Impulse + Step Load	Impulse + Ramped Step Load
Steel	Unperforated	0.7	0.4
Steel	Square	1.2	0.7
Steel	Triangular	1.5	1.1
Al (unwelded)	Unperforated	1.8	0.8
Al (unwelded)	Square	2.7	1.7
Al (unwelded)	Triangular	3.6	2.6
Al (welded)	Unperforated	1.9	0.9
Al (welded)	Square	2.9	1.8
Al (welded)	Triangular	3.9	2.7

**Case II: Radius = 3.0 m**

Material	Port Pattern	Minimum Thickness (cm)	
		Impulse + Step Load	Impulse + Ramped Step Load
Steel	Unperforated	0.5	0.4
Steel	Square	0.5	0.4
Steel	Triangular	0.5	0.4
Al (unwelded)	Unperforated	1.0	0.9
Al (unwelded)	Square	1.0	0.9
Al (unwelded)	Triangular	1.0	0.9
Al (welded)	Unperforated	1.1	0.9
Al (welded)	Square	1.1	0.9
Al (welded)	Triangular	1.1	0.9

Table 3.4. Minimum Thicknesses Needed for Lifetimes of 6, 9, 12 and 30 Years.

**Case I: Radius = 1.5 m**

Material	Port Pattern	Minimum Thickness (cm)	
		Impulse + Step Load	Impulse + Ramped Step Load
Steel	Unperforated	2.9	1.6
Steel	Square	4.5	2.5
Steel	Triangular	6.1	3.7
Al (unwelded)	Unperforated	7.2	3.9
Al (unwelded)	Square	11.3	4.8
Al (unwelded)	Triangular	15.6	8.0
Al (welded)	Unperforated	8.3	4.3
Al (welded)	Square	13.0	4.8
Al (welded)	Triangular	20.7	10.8

**Case II: Radius = 3.0 m**

Material	Port Pattern	Minimum Thickness (cm)	
		Impulse + Step Load	Impulse + Ramped Step Load
Steel	Unperforated	2.0	1.6
Steel	Square	2.0	1.6
Steel	Triangular	2.0	1.6
Al (unwelded)	Unperforated	4.6	3.7
Al (unwelded)	Square	4.6	3.8
Al (unwelded)	Triangular	4.6	3.8
Al (welded)	Unperforated	4.9	4.0
Al (welded)	Square	4.9	4.0
Al (welded)	Triangular	4.9	4.0

## 4. Target Support Structure

A significant effort has not been devoted to the consideration of target positioning and cooling. Therefore, a target positioner or a cryogenic system has not yet been designed. Only more general thoughts and some options can be provided at this time. Two approaches have been considered: one based on the systems developed for the NOVA laser and one similar to what is normally proposed for ICF reactors.

### 4.1. Positioning

Two approaches can be taken to target positioning. The ultimate choice of a positioning system will have to reflect target alignment requirements. These positioning requirements will depend upon target design, beam optics and target diagnostics.

The first approach is to build upon the target positioning developments in the laser fusion program [?, ?]. This would be a mechanical positioner coupled to Target Alignment Viewers (TAV's) such as those developed for NOVA. The NOVA TAV's can determine the position and orientation of a target to within several  $\mu\text{m}$ , which is approximately the backlash on the positioner. It is not clear that light ion beam targets require such positioning accuracy. An issue for such a system would be its survival in the presence of a high yield shot. The TAV's could be removed prior to the shot and the positioner would be designed so that only a replaceable holder would be destroyed. However, the holder would become potentially damaging shrapnel.

The second approach is to develop a target injector to propel the target into the chamber from the outside and a tracking system to time the firing of the driver to the arrival of the target at the beam focus. This is the approach proposed in ICF reactor designs. The LIBRA study [?] used a pneumatic gun design to inject the target. Target survival during injection and target tracking with lasers have been analyzed. The gun dispersion would have to be matched to the tolerances in the target position dictated by target design and beam optics. Target orientation is a persistent problem that could be solved by spinning the target with

rifling in the gun's barrel if the target has azimuthal symmetry. It would be difficult or impossible to provide structures external to the target, such as x-ray backlighters, with this approach. This approach reduces the problem of shrapnel and has the advantage of being relevant to ICF reactors.

With the advantages and disadvantages of both approaches, it may be appropriate to develop both. The NOVA approach would be best during target development. During high yield production shots, target diagnostics may not be required and the injection approach could be used.

## 4.2. Cryogenics

The cryogenic system is required to keep the fuel targets within the targets in the proper state. The actual temperature at which the DT fuel must be held is determined by target design. If the target uses liquid DT held in place by a low density plastic or glass foam, then the fuel temperature must be above 20 K; if solid DT is used, then it must be below 20 K. The density of DT gas in the central void is a target design parameter that will further define the fuel temperature.

The two approaches to target positioning lead to differences in the cryogenic systems. For the NOVA positioning system, a cryogenic system was designed several years ago [?]. This system uses a Cryogenic Utility Post (CUP) that makes contact with the target on one end and the cryostat on the other end. Additionally, cold helium can be blown onto the target to provide greater cooling. A shroud covers the target to channel the gas flow around the target and to protect the target from radiant heating from the 300 K target chamber. The shroud would be retracted shortly before the target shot. The target positioning system would act on the target through the CUP. This system would have the problem of shrapnel mentioned above.

For target injection with a gun, the target would be cooled in a system back in the gun. The important issue is heating of the target during injection. The DT fuel must be at

the proper temperature at the time it reaches the ion beam focus. The approach calls for placing the targets in sabots that protect them from frictional heating while in the gun. The sabots, which are made from pieces of low conductivity plastic, disassemble in the target chamber and separate from the targets. Frictional and radiant heating of the target as it moves from the point of separation from the sabot to the focus of the ion beams must be considered. Heating due to the decay of tritium in the fuel is also an issue.

The condensation of target chamber fill gas onto the target is a concern for both approaches. Helium was chosen as a target chamber fill gas partially to avoid this problem. The boiling point of helium is 4 K, which is probably below the temperature of the target surface. There would be a condensation problem with any other target chamber fill gas.

## **5. Post-Shot Operations**

### **5.1. Radioactivity**

A 1-dimensional analysis has been made of the neutron transport, activation, and gamma ray transport in the LMF target chamber [?]. The ONEDANT [?] neutron transport code was used to calculate the propagation of neutrons from the target to the LMF target chamber structures. The neutron spectrum is based upon the predictions for the HIBALL target [?]. Radioactivity induced in the structure is calculated with the DKR-ICF code [?]. The dose rate is then calculated at a given position. Using ONEDANT to transport the gamma rays from the activated material to a given position, the dose rate at that position is then calculated. It is assumed that the average target yield is 200 MJ and that 500 are shot in a year. The pulsing scheme is 2 shots a day, separated by 6 hours, with 18 hours between that last shot of the day and the first shot of the next day. Operations continue in this manner 5 days a week for 50 weeks and then the facility is shut down for maintenance. The dose rate at the outside edge of the target chamber is shown in Fig. 5.1 plotted against time. The results are plotted versus time for 150 cm radius target chambers made of three materials: aluminum 5083, aluminum 6061, and 2 1/4 Cr-1 Mo steel. For these calculations

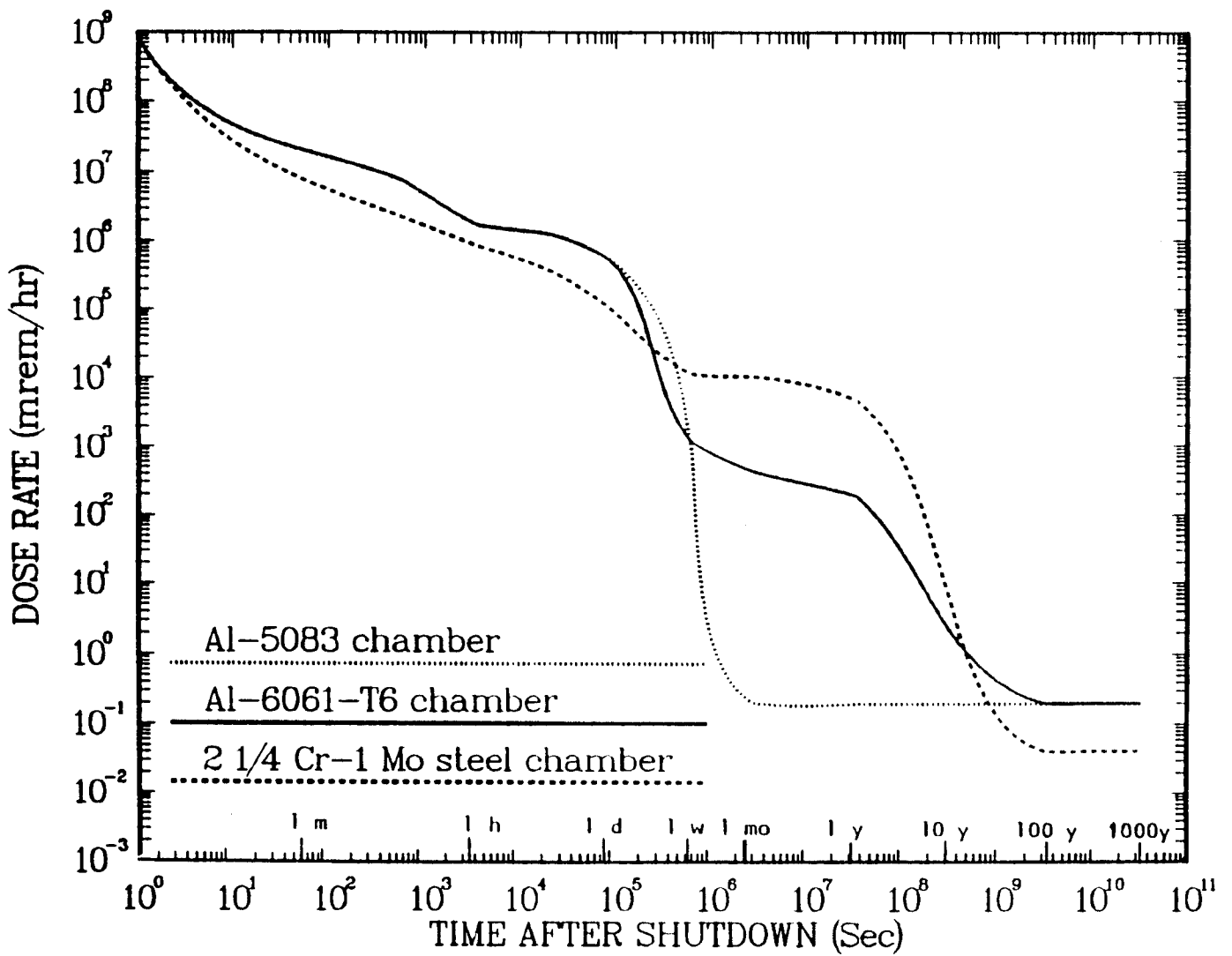


Figure 5.1. Comparison between contact dose rates behind the chamber wall.

the aluminum walls are assumed to be 6 cm thick and the steel walls are 3 cm thick. In all cases the walls are lined externally with 1 cm of Boral and are surrounded by a 241 cm thick borated water shield. In Fig. 5.1, it can be seen that out to 1 day after shutdown the two aluminum alloys are the same and are much higher than the steel. At 1 week, all walls have the same dose rate. From one week out to ten years aluminum 5083 is much better than the other two materials. The dose rate calculations for all of the first wall thicknesses determined in Chapter 3 have not been completed.

Activated target debris and unburned tritium also contribute to the radioactivity. The activation of the target itself by fusion neutrons has been determined [?]. Specifically, studies have been made of the effect of the choice of outer shell material on the level of radioactivity produced. The LLNL ion beam target design [?] was used in this study. This target calls for a high atomic number outer shell, which accounts for most of the induced radioactivity. Lead, gold and tungsten were considered as outer shell materials. The inside of the target consists of a DT capsule surrounded by low density, low atomic number material. Carbon and hydrogen (plastic), lead and lithium ( $\text{Pb}_5\text{Li}_{95}$ ), and beryllium and oxygen ( $\text{BeO}_2$ ) were considered for this low atomic number material. The ANISN [?] neutron transport code and the DKR[?] activation code were used in this study to obtain the results shown in Fig. 5.2. For these results it was assumed that there was 1 mg of DT, a fuel  $\rho_r$  of  $2 \text{ g/cm}^2$ , and a burnup fraction of 30%, which is equivalent to a yield of 100 MJ. Results can be approximately linearly scaled to other yields. The only effects of varying the low atomic number material occur in the first few minutes after the target explosion and are therefore not important. In Fig. 5.2, one can see that there is a significant effect from the choice of the shell material. Gold produces more than an order of magnitude more radioactivity than the others up to 1 week after the shot and tungsten is the worst beyond 1 month. Lead clearly produces the least amount of radioactivity and would be the best choice of material as long as the target performance is not impeded. The radioactivity from tritium

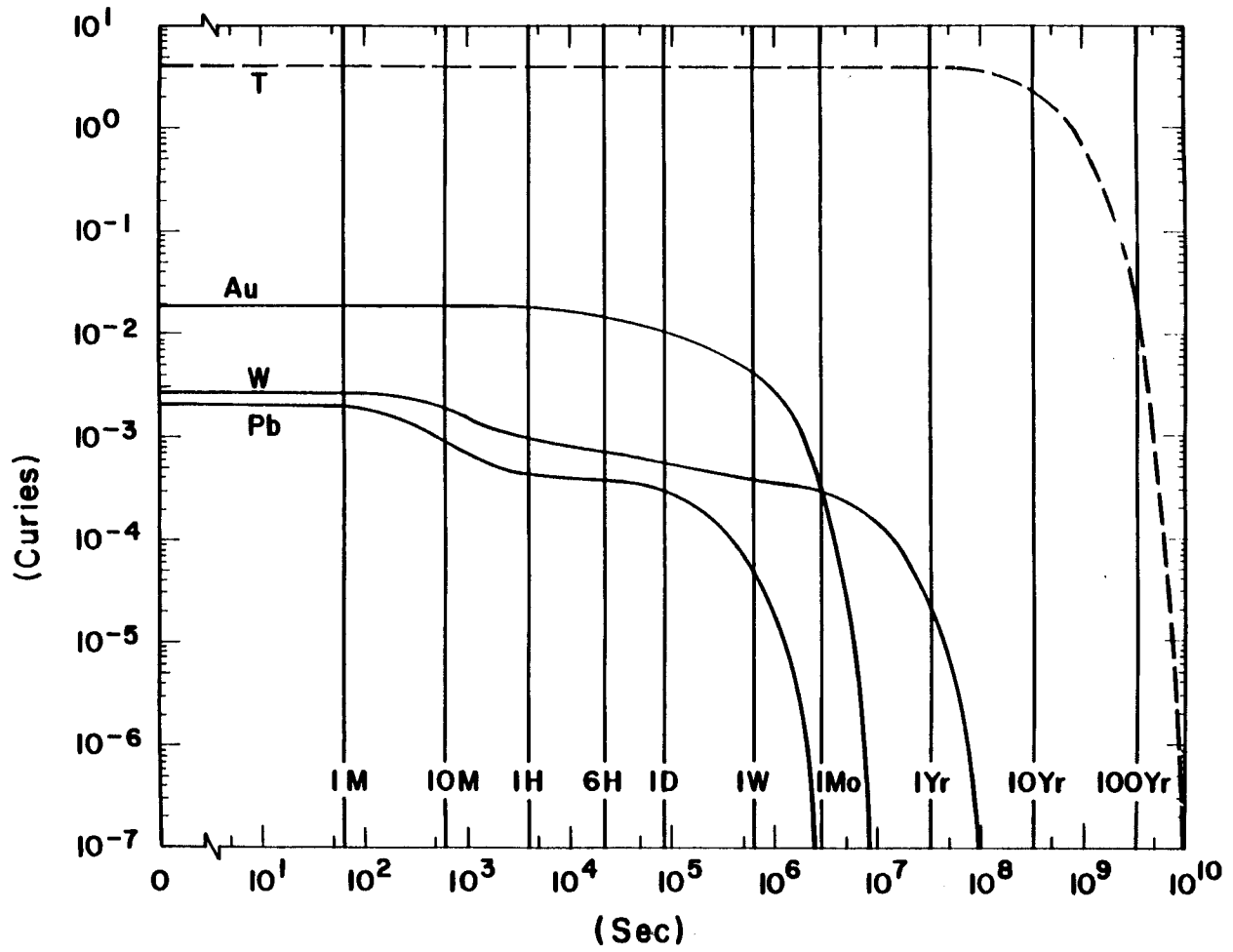


Figure 5.2. Comparison of target debris radioactivity for outer shells of various materials.

is shown to be much larger than that from induced radioactivity from outer shells of all three materials. The dose rate from these two sources has not been calculated because it is not known where the activated material is deposited. The tritium may be pumped out of the chamber after each shot for venting or recovery. It is necessary to determine where the debris material is deposited and if it can be removed. It may become attached to the the vaporized graphite in the chamber and will deposit wherever the graphite does. This is a possible method of removing the target debris from the chamber.

## **5.2. Reentry**

Reentry into the target chamber area by maintenance personnel can only be performed after a cooldown time to reduce the dose rate to acceptable levels. If one operates for a year and uses the dose rate at the outside surface of the chamber as a measure, the cooldown time is determined by the calculations presented in the preceding section. The choice of an acceptable dose rate is very important in determining the cooldown time. If we use 2.5 mrem/hr as an acceptable dose rate and the wall is made of aluminum 5083 the cooldown time would be about 2 weeks. If we instead allow each worker to receive 1.25 rem in a 40 hr work week, then the cooldown time is reduced to slightly more than a week. As discussed above, there is also the question of tritium and target debris. It is assumed that all such materials can be removed before reentry.

## **5.3. Recovery and Refurbishing**

Remote reentry is needed to perform tasks in the target chamber between periodic shutdowns for maintenance. The tritium would be pumped out of the target chamber and the chamber opened to allow remote manipulators to descend into the target chamber. In this way, experiments can be arranged and repairs to the target chamber can be performed.

## 6. Fragmentation

A topic related to x-ray vaporization of first wall material is x-ray generated fragmentation of other structures in target chambers and the acceleration of such fragments as shrapnel. Some analytic models of fragmentation have been coupled with an x-ray generated shock formalism to develop a means of estimating the size and speed of the shrapnel fragments. Estimates have been made of the shrapnel parameters for two types of structures that could be in the target chamber. The effects of the resulting shrapnel on the target chamber wall have not been estimated.

Fragmentation is considered to be a two step process: 1) x-rays generate a large pressure gradient in the material which causes the material to move, and 2) this motion provides kinetic energy, some of which can be converted into the surface energy required for fragmentation. Step 1 can be modeled by a method described elsewhere [?]. For step 2, the methods of Dennis Grady of SNL [?] have been used.

The expression for the pressure is valid as long as the deposition length is less than  $C_s \Delta t$ , where  $C_s$  is the speed of sound in the unvaporized material and  $\Delta t$  is the width of the x-ray pulse. The pressure is proportional to  $\sin \alpha$ , where  $\alpha$  is the angle between the direction of the x-rays and the surface of the material. For graphite, it was found by comparison with computer simulations and experiment[?] that the pressure from an x-ray intensity of  $I_x$  is

$$P = 0.38 I_x \sin \alpha / C_s \quad (1)$$

The velocities of the shrapnel fragments are determined by conservation of momentum. If the thickness of the material is  $T$  and the mass density is  $\rho$ , its areal mass density is  $\rho T$ . The impulse is  $P \Delta t$ , which is the momentum gained by the material. Therefore, the velocity of the material is independent of the size of fragments into which it is broken, and can be expressed as,

$$v_{frag} = 0.38 I_x \sin \alpha \Delta t / \rho T. \quad (2)$$

Finally, it is necessary to calculate the sizes of the fragments. The Grady model allows some of the kinetic energy about the center of mass of a piece of material that is to become a fragment to be converted into the surface energy of the fragment. For a solid, this model predicts that the average diameter of a fragment is

$$d = 2.72(K_{Ic}/\rho\dot{\epsilon}C_s)^{2/3}. \quad (3)$$

Here,  $K_{Ic}$  is the fracture toughness, which for graphite is between  $3 \times 10^8$  and  $3 \times 10^9$  dyne/cm<sup>3/2</sup>. The larger value is more conservative because it will lead to larger, more damaging shrapnel.

This formalism was used to consider the fragmentation into shrapnel of two different structures. Both structures are assumed to be in an LMF target chamber where they are subjected to the x-rays from a 1000 MJ target microexplosion.

First a sphere of graphite, concentric with the target was considered. For a sphere,  $\alpha$  is  $90^\circ$  and the strain rate is

$$\dot{\epsilon} = 2v_{frag}/3R, \quad (4)$$

where  $R$  is the distance between the target and the inside of the graphite sphere. Therefore, the fragment diameter is

$$d = 4.53 \times 10^7 R^2 T^{2/3} \text{ (cm)}. \quad (5)$$

Some results are tabulated in Table 6.1 for a graphite sphere, with  $T = 0.1$  cm and for  $R$  from 10 to 100 cm. In addition to the fragment velocities and diameters, the fragment mass,  $M_{frag}$ , and momentum,  $Mom_{frag}$ , are listed. Notice that the momentum of each fragment increases with distance from the target.

The second structure considered was a hollow graphite cylinder pointed directly at the target. Here,  $\sin \alpha$  is not constant, but is a function of the tube's radius and the distance that part of the tube is from the target,

$$\sin \alpha = r_{tube}/(r_{tube}^2 + R^2)^{1/2}. \quad (6)$$

Table 6.1. Fragment Parameters for a Sphere of Graphite Concentric with Targets in LMF Target Chamber.

R (cm)	$v_{frag}$ (m/s)	d (cm)	$M_{frag}$ (g)	$Mom_{frag}$ (g-cm/s)
10	2130	$1.0 \times 10^{-5}$	$9.6 \times 10^{-15}$	$2.0 \times 10^{-9}$
20	1070	$3.9 \times 10^{-5}$	$5.8 \times 10^{-13}$	$6.2 \times 10^{-8}$
50	430	$2.4 \times 10^{-4}$	$1.3 \times 10^{-10}$	$5.6 \times 10^{-6}$
100	213	$1.0 \times 10^{-3}$	$9.6 \times 10^{-9}$	$2.0 \times 10^{-4}$

Table 6.2. Fragment Parameters for Graphite Tube in LMF Target Chamber.

R=	10 cm	20 cm	50 cm	100 cm	150 cm
P (GPa)	496	124	20	5.0	2.2
$v_{frag}$ (m/s)	2160	540	86	22	9.6
d (cm)	0.033	0.133	0.833	†	†
$M_{frag}$ (mg)	0.36	22.8	5578	†	†
$Mom_{frag}$ (g-cm/s)	77	1232	$4.8 \times 10^4$	†	†

†Fragment sizes are larger than validity limits of the model.

It is assumed that the tube's radius,  $r_{tube}$ , is greater than the target radius, so that the target can be treated as a point source of x-rays. This insures that the x-rays will deposit on the inside surface of the tube and the tube will fragment due to rapid outward expansion. The pressure driving this expansion is, if  $R \gg r_{tube}$ ,

$$P = 4.96 \times 10^7 r_{tube} / R^2 \text{ (MPa)}. \quad (7)$$

The velocity at which the tube cylindrically expands is,

$$v_{frag} = 2.16 \times 10^5 r_{tube} / TR^2 \text{ (cm/s)}. \quad (8)$$

For a cylindrical expansion, the strain rate is

$$\dot{\epsilon} = v_{frag} / 3r_{tube}. \quad (9)$$

From the preceding equations, the fragment diameter is

$$d = 7.18 \times 10^{-3} T^{2/3} R^2 \text{ (cm)}. \quad (10)$$

For  $r_{tube} = 1$  cm and  $T = 0.01$  cm, the pressure, and the fragment speed, diameter, mass, and momentum are listed in Table 6.2. Once again, notice that the momentum of a fragment increases as the distance from the target. The fragment speed falls off rather quickly because of the variation in  $\sin \alpha$ .

## 7. First Wall Material Experiments

A long-standing problem in the technology development of ICF in general and the LMF in particular is the behavior of materials that are subjected to intense x-rays. In light ion beam fusion, where ballistic propagation of ions is used, the final transport optics must be close enough to the target that the materials will be subjected to intense x-ray pulses from the target. Additionally, in the LMF the x-rays must be allowed to propagate for the simulation experiments to work, so the target chamber wall would have to be many meters

from the target explosion to avoid x-ray intensities high enough to vaporize. Therefore, the behavior of materials which absorb these intense x-rays is important to understand. This is discussed in Chapter 2, where the results of a computational study are presented. In this chapter, the experimental studies are discussed.

### **7.1. Experiments on SATURN**

SATURN is a high power electron accelerator that can create intense pulses of x-rays. When used in a gas pinch mode, SATURN can create as much as 100 kJ of roughly 1 keV x-rays in a pulse as short as 10 ns. The total energy in x-rays is as high as 500 kJ, much of it being in photons of less than 0.5 keV in energy. The pulse width for the total x-ray spectrum is 100 ns. The spectrum of x-rays and the pulse width is affected by the gas used in the pinch. X-rays from pinches formed in neon and argon have been used. The x-ray spectra are shown in Figs. 7.1 and 7.2 for these two gases. Samples of various materials can be placed as close as 3.8 cm from the x-ray source, leading to fluences of greater than 0.5 keV x-rays as high as 550 J/cm<sup>2</sup> and total fluences as high as 2750 J/cm<sup>2</sup>. The fluences and intensities achievable on SATURN are compared with LMF conditions in Table 7.1. The LMF conditions are consistent with the two designs discussed in this report. The spectrum of x-rays in the LMF is as discussed in Chapter 2, which differs from spectra generated in SATURN in the lack of photons below a few hundred eV. The pulse width of target generated x-rays is about 1 ns. Because of the disparity in the pulse widths, the intensities possible in SATURN are well below those expected on the LMF walls even though the fluences are comparable. Whether the total or the greater than 0.5 keV values are more important depends on the material being irradiated. Since carbon has similar stopping powers for 0.3 and 1 keV photons, the total fluence is most useful for graphite. On the other hand, aluminum has a very different stopping length for the two photon energies, so the greater than 0.5 keV fluence is more relevant. In experiments on SATURN, the low

Table 7.1. Comparison of LMF and SATURN X-ray Conditions.

	SATURN Neon	SATURN Argon	LMF 150 cm	LMF 300 cm
Distance (cm)	3.8	3.8	150	300
Total Energy	500 kJ	500 kJ	200 MJ	200 MJ
Energy $\geq$ 0.5 keV	100 kJ	40 kJ	200 MJ	200 MJ
Total Fluence (J/cm <sup>2</sup> )	2750	2750	700	180
Fluence $\geq$ 0.5 keV (J/cm <sup>2</sup> )	550	220	700	180
Total Pulse Width (ns)	20	10	1	1
Pulse Width $\geq$ 0.5 keV (ns)	100	100	1	1
Total Intensity (GW/cm <sup>2</sup> )	5.5	2.2	700	180
Intensity $\geq$ 0.5 keV (GW/cm <sup>2</sup> )	27.5	22.0	700	180

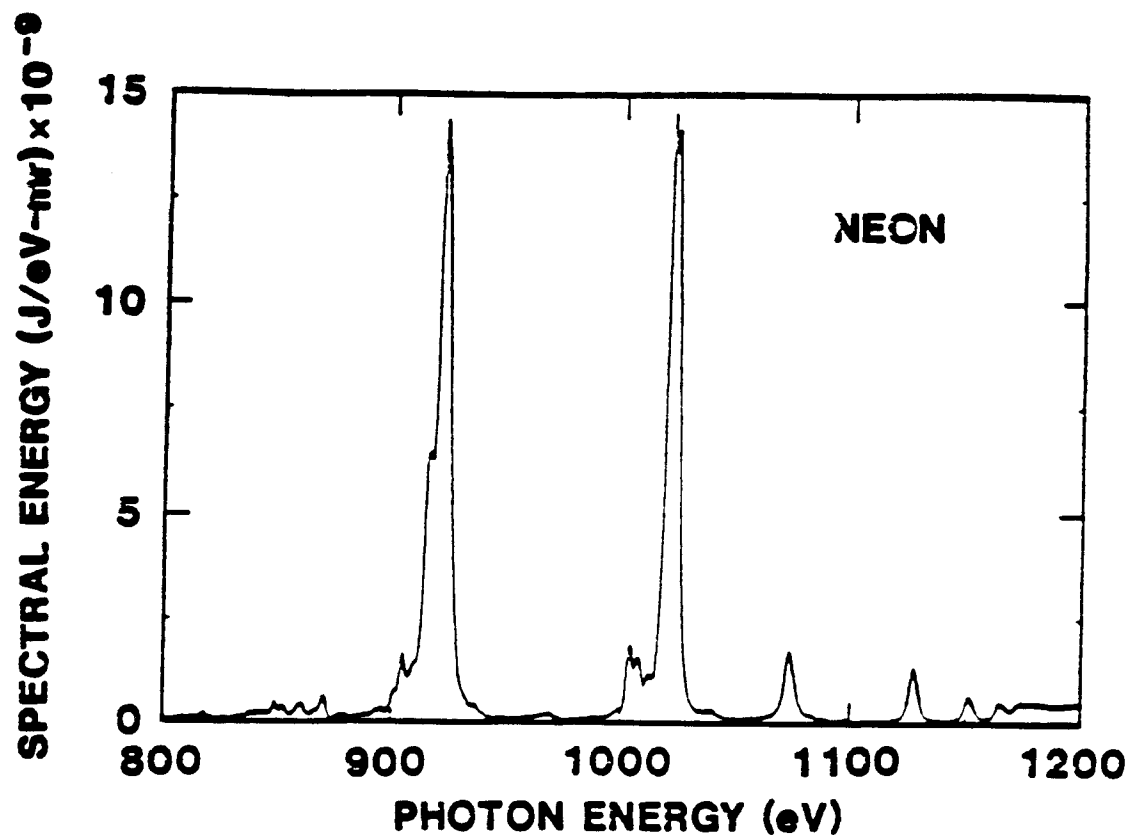


Figure 7.1. Spectrum from neon gas pinch on SATURN.

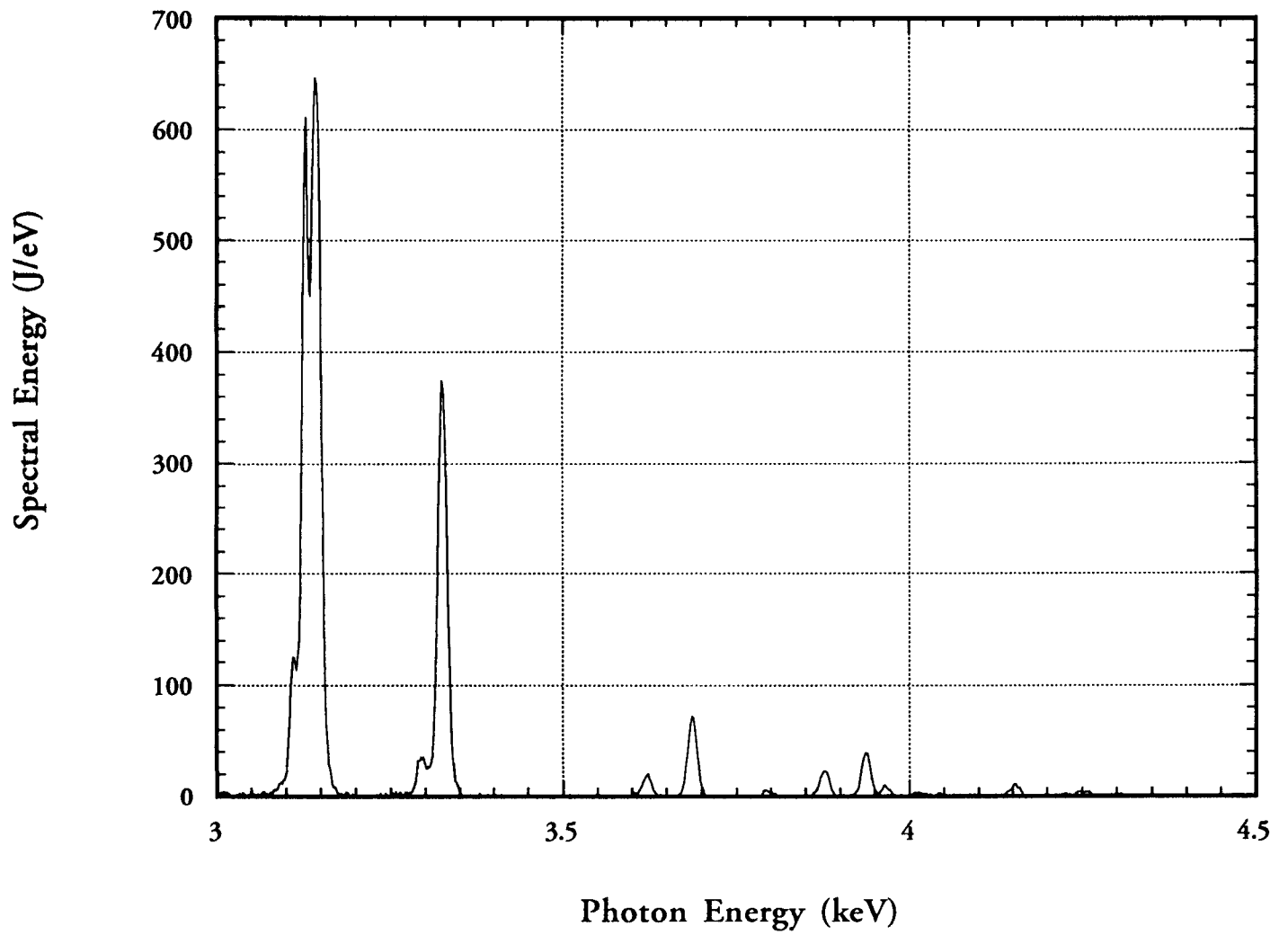


Figure 7.2. Spectrum from argon gas pinch on SATURN.

energy photons may be filtered out by placing an aluminum foil between the pinch and the sample.

Two types of experiments have been carried out on SATURN: survival and shock propagation. In the survival experiments, material samples are irradiated to determine whether they can survive a single shot of SATURN x-rays. These samples can later undergo microstructural analysis to determine how the x-rays have changed the material. Shock propagation experiments involve the placement of strain gages at the back of the samples that can measure the waveform and time-of-arrival of the x-ray induced shock.

#### **7.1.1. Survival Experiments**

Over the past three years, several materials have been irradiated on SATURN without active diagnostics (i.e., without strain gages). Most results have been reported elsewhere, so only Tables 7.2 and 7.3 and Figs. 7.3 and 7.4 will summarize them. In addition to results listed in these tables, the 4-directional woven graphite has been re-exposed to additional shots with argon produced x-rays. Although the sample is still undamaged, it may not be exposed further because of potential beryllium contamination.

#### **7.1.2. Shock Propagation Experiments**

With a great deal of help from scientists at SNL, experiments were initiated on SATURN in May 1990 to actively measure the propagation of x-ray generated shocks through aluminum. The purpose of this was to test the ability to simulate this process with the CSQ code. There were four aluminum 6061 samples shot in May of 1990 with strain gages mounted on their back surfaces. The samples were roughly 3 mm thick, 1 inch diameter disks. The samples were machined on the backs to allow proper mounting of the quartz strain gages. Unfortunately, the sample thicknesses were not measured after this machining, so the exact thicknesses of the samples were unknown. The samples are still in hand, but since some material was vaporized off of the surface, the thickness cannot be remeasured.

Table 7.2. Samples of LMF First Wall Materials Irradiated with Neon Pinch X-rays on SATURN.

Shot No.	Material	Total X-ray Energy Fluence (J/cm <sup>2</sup> )	Greater than 900 eV Energy Fluence (J/cm <sup>2</sup> )	Pulse Width (ns)	Result
658	Graphite H-451 fine grained	1900	440	21	destroyed powder
658	Alumina coated aluminum 6061	1900	440	21	survived
664	Graphnol fine grained graphite	1600	370	18	destroyed six pieces
665	Graphite A05 short random fibers in a carbon matrix	2200	510	13	destroyed nothing left
669	K-Karb 2-D woven graphite in a carbon matrix	3400	730	16	survived delaminated
669	Graphite CGW fine grained	3400	730	16	destroyed powder
669	Graphite AJT fine grained	3400	730	16	destroyed powder
669	Dunlop breakpad graphite fibers in a carbon matrix	3400	730	16	destroyed shredded

Table 7.3. Samples of LMF First Wall Materials Irradiated with Argon Pinch X-rays on SATURN.

Shot No.	Material	Total X-ray Energy Fluence (J/cm <sup>2</sup> )	Greater than 900 eV Energy Fluence (J/cm <sup>2</sup> )	Pulse Width (ns)	Result
736	Bare aluminum 6061	2204	242	16	survived
736	Carbon coated aluminum 6061	2204	242	16	survived
736	Stapleknit graphite	2204	242	16	destroyed delaminated
737	4-D woven graphite (FMI)	2039	209	16	survived
739	3-D random fiber graphite	2673	237	11	destroyed
737	A05 Graphite fine grained	2039	209	16	survived
739	2-d woven graphite (unfiltered)	2673	237	11	destroyed
739	2-d woven graphite (filtered)	237	237	11	survived
737	Graphite carpet	2039	209	16	survived

# SATURN Irradiated LMF First Wall Sample Materials

(x-rays from Neon gas pinches)

Graphite  
H 451



Al 6061  
coated with Alumina



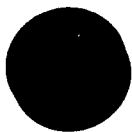
Graphite  
Graphnol N3M



Graphite  
A05

(nothing left)

Graphite  
K Karb  
(2 D weave)



Graphite  
CGW



Graphite  
ATJ



Graphite  
Dunlop breakpad



SAMPLE HOLDER



TYPICAL PARAMETERS

Spectrum - 1 keV lines

Fluence - 500 J/cm<sup>2</sup>

Pulse Width - 15 to 20 ns

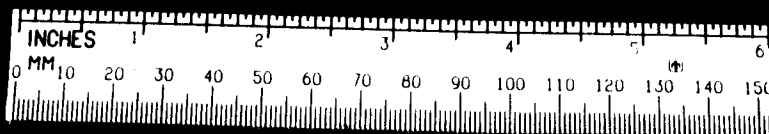


Figure 7.3. Photograph of samples irradiated with SATURN neon pinch x-rays.

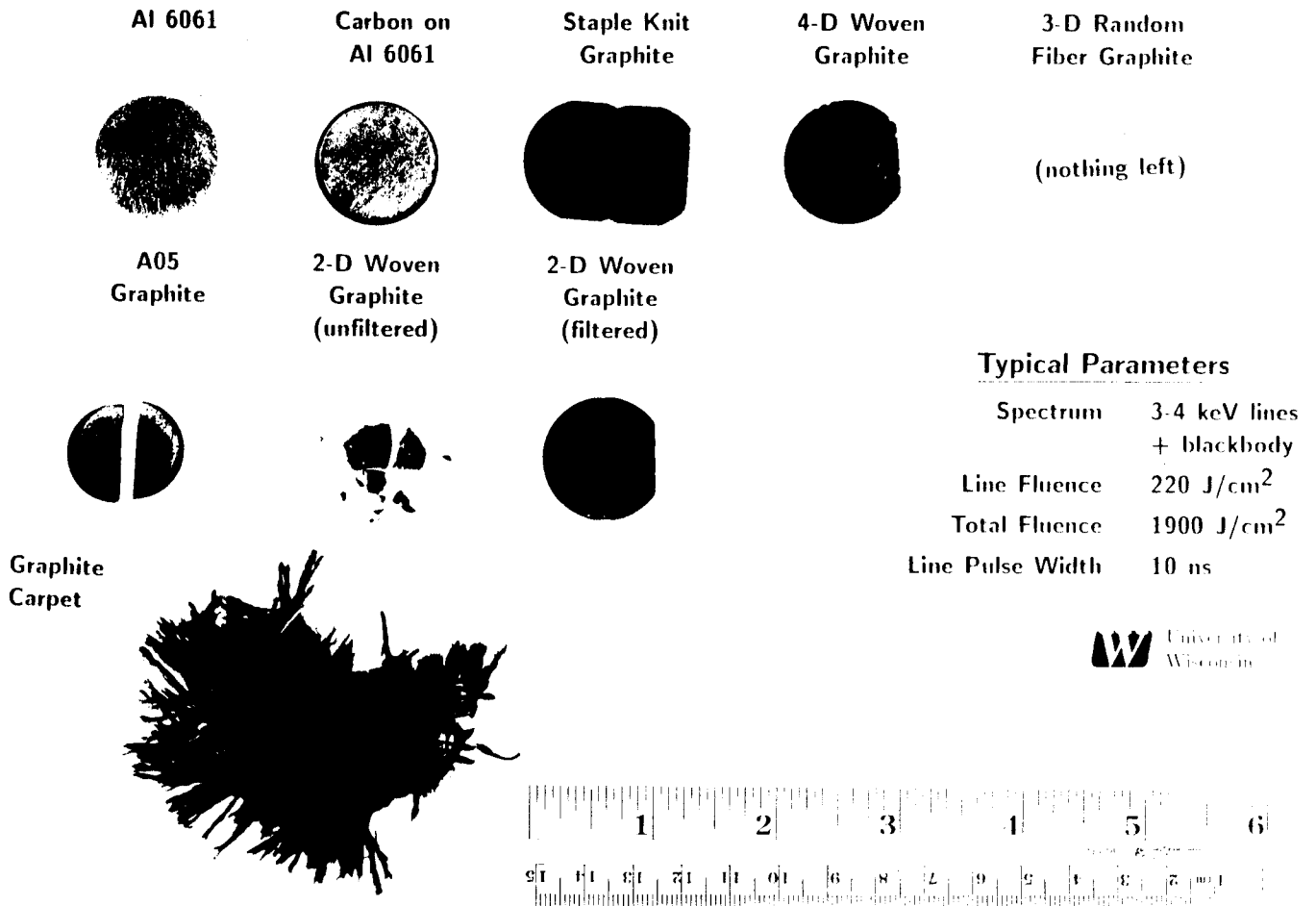


Figure 7.4. Photograph of samples irradiated with SATURN argon pinch x-rays.

The measured strain gage signals are shown in Figs. 7.5 through 7.8. Four samples were all irradiated on the same shot, 936. The samples were all placed 3.8 cm from the center of the argon pinch. This shot generated 350 kJ of x-rays below 1 keV and 33 kJ above 1 keV. Therefore, the total x-ray fluence on the samples was 2100 J/cm<sup>2</sup> and the fluence above 1 keV was 182 J/cm<sup>2</sup>. The x-ray power for photons greater than 1 keV is shown as a function of time in Fig. 7.9. The total x-ray power is shown in Fig. 7.10. The pulse width was 13.5 ns for the greater than 1 keV photons. The pulse width of the total x-ray spectrum is about 70 ns. Two of the samples were coated with Television Tube Coat, a mixture of graphite powder and lacquer manufactured by GC Electronics of Rockford, IL as spray-on. It is believed that this coating was about 100  $\mu\text{m}$  thick, though the thickness was not measured. Two of the samples were not coated, but were polished to a smoothness of about 1  $\mu\text{m}$ . Of these four samples, two were irradiated by x-rays filtered with a thin aluminum foil and two were irradiated with unfiltered x-rays. The effect of the filtering is the removal of photons below 1 keV from the spectrum. The choices made for each sample are shown in Table 7.4.

It can be seen that there there is a great deal of noise in the signals. This is due to the strain gage reacting to the electromagnetic noise in the vacuum chamber of SATURN. Recent experiments have shown that this noise can be removed from the measured signal by shielding. The first large negative peak is due to Bremsstrahlung induced in the feeds to the SATURN diode, and can serve as a fiducial. If the thickness of the sample is 3 mm and if the speed of sound in aluminum 6061 is 5.35 mm/ $\mu\text{s}$ , the stress wave should arrive at the gage about 560 ns after the x-rays are deposited in the material. The peak of the hard x-rays occurs about 50 ns after the peak of the current in the feeds. So the shock passing through the samples should be measured on the strain gages about 610 ns after the fiducial. The delay times after the fiducial for the largest positive signal are shown in Table 7.4. For both 936A and 936C, the signal from the strain gage ends before the shock pressure on the

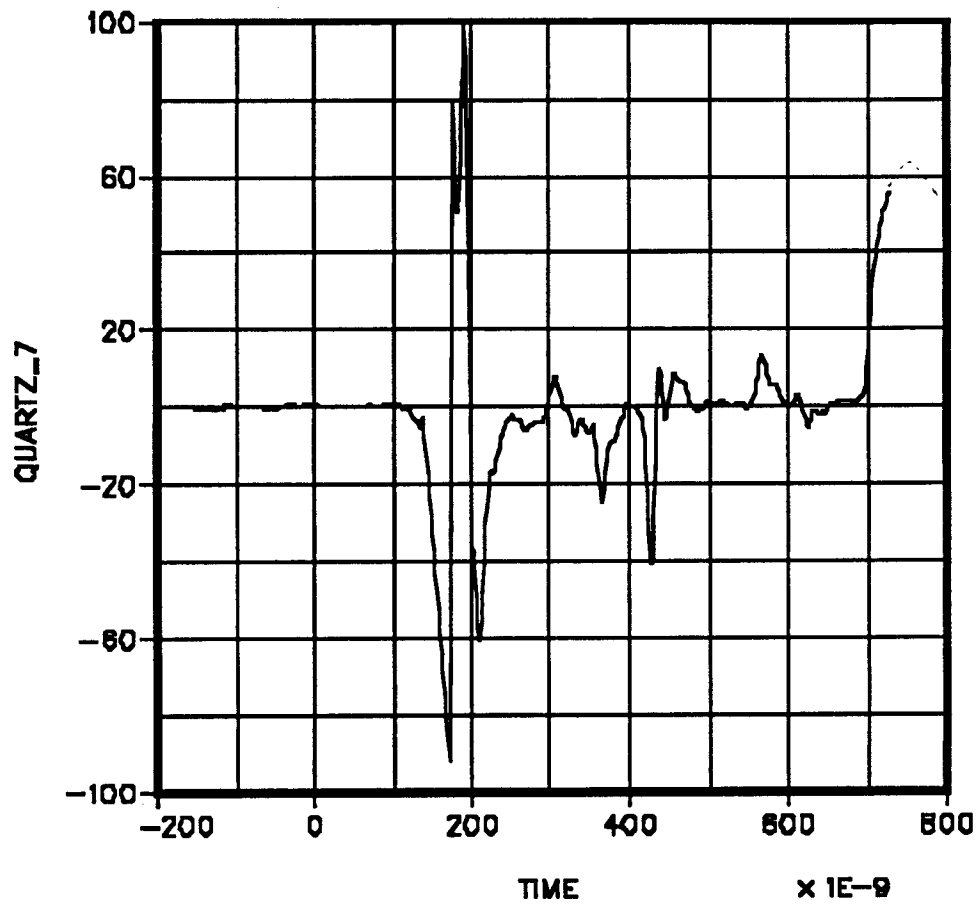


Figure 7.5. Strain gage signal measured at back of Sample 936A. Sample is uncoated and unfiltered.

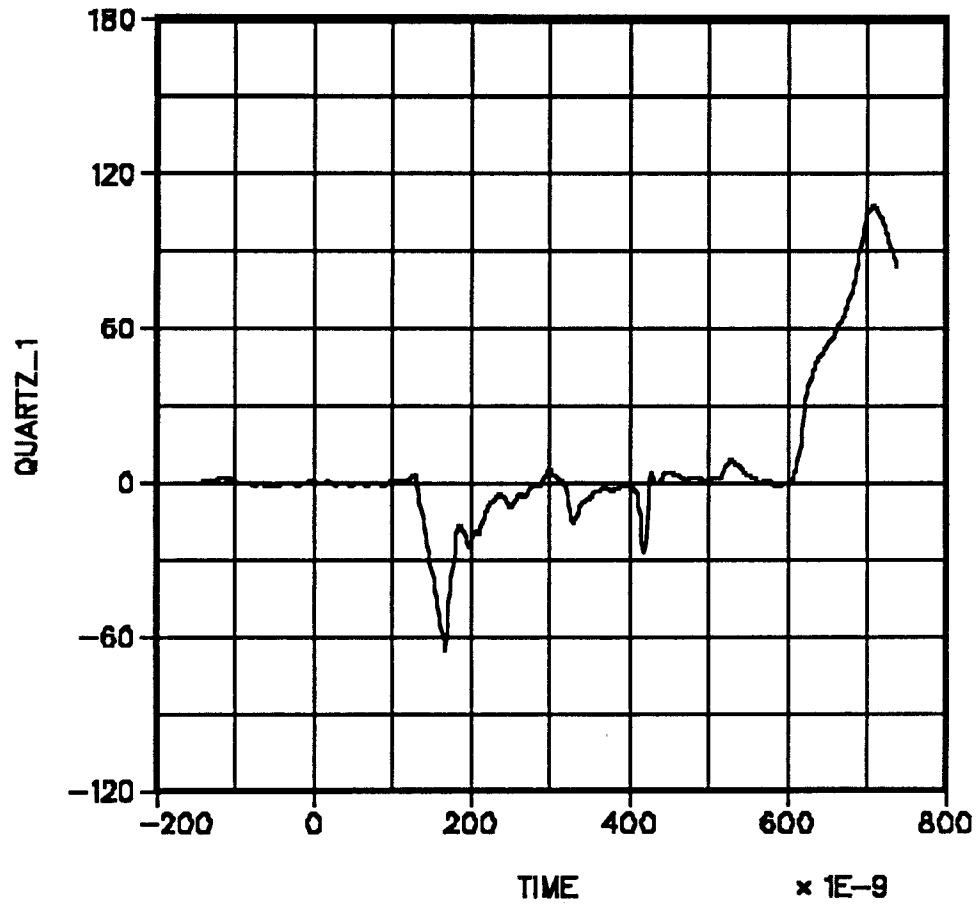


Figure 7.6. Strain gage signal measured at back of Sample 936B. Sample is uncoated and filtered.

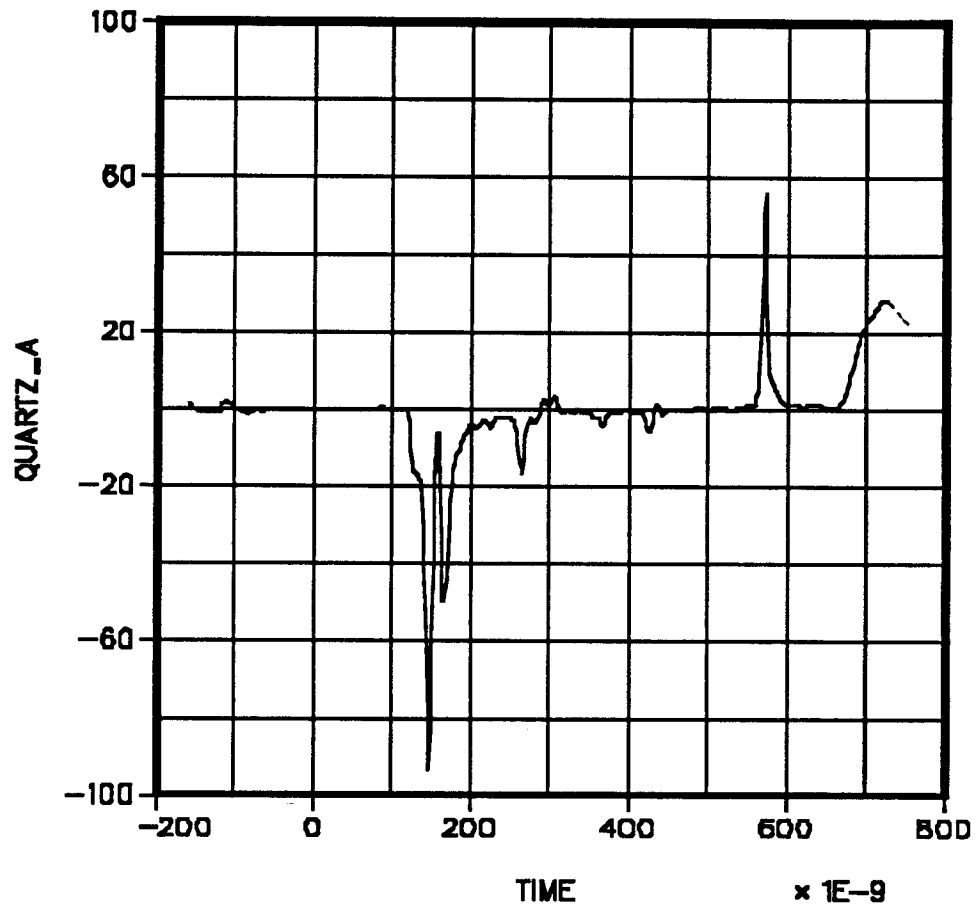


Figure 7.7. Strain gage signal measured at back of Sample 936C. Sample is coated and unfiltered.

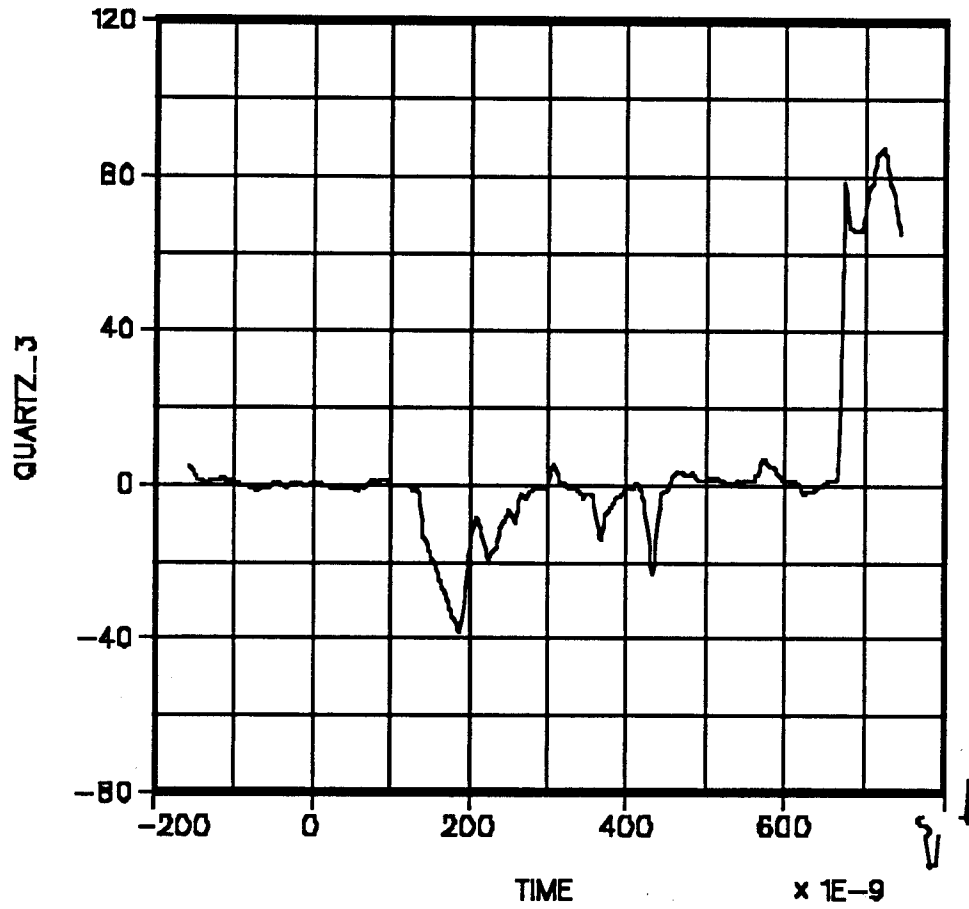


Figure 7.8. Strain gage signal measured at back of Sample 936D. Sample is coated and filtered.

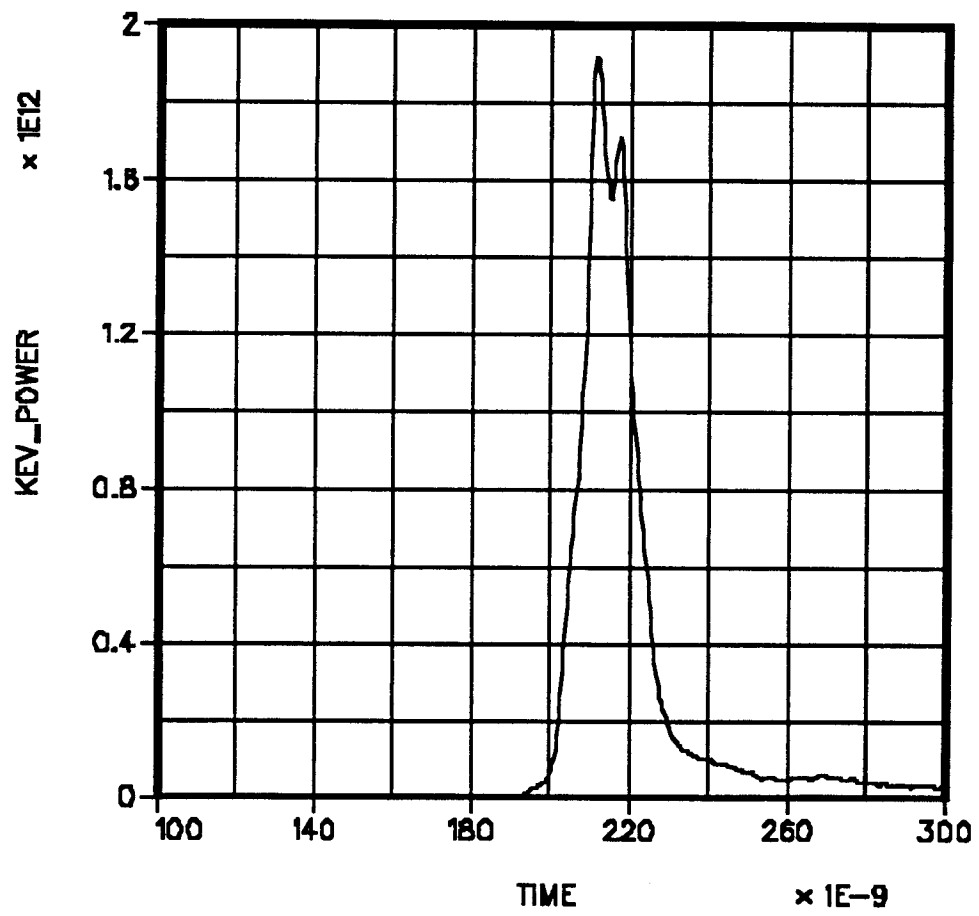


Figure 7.9. X-ray power of greater than 1 keV photons versus time.

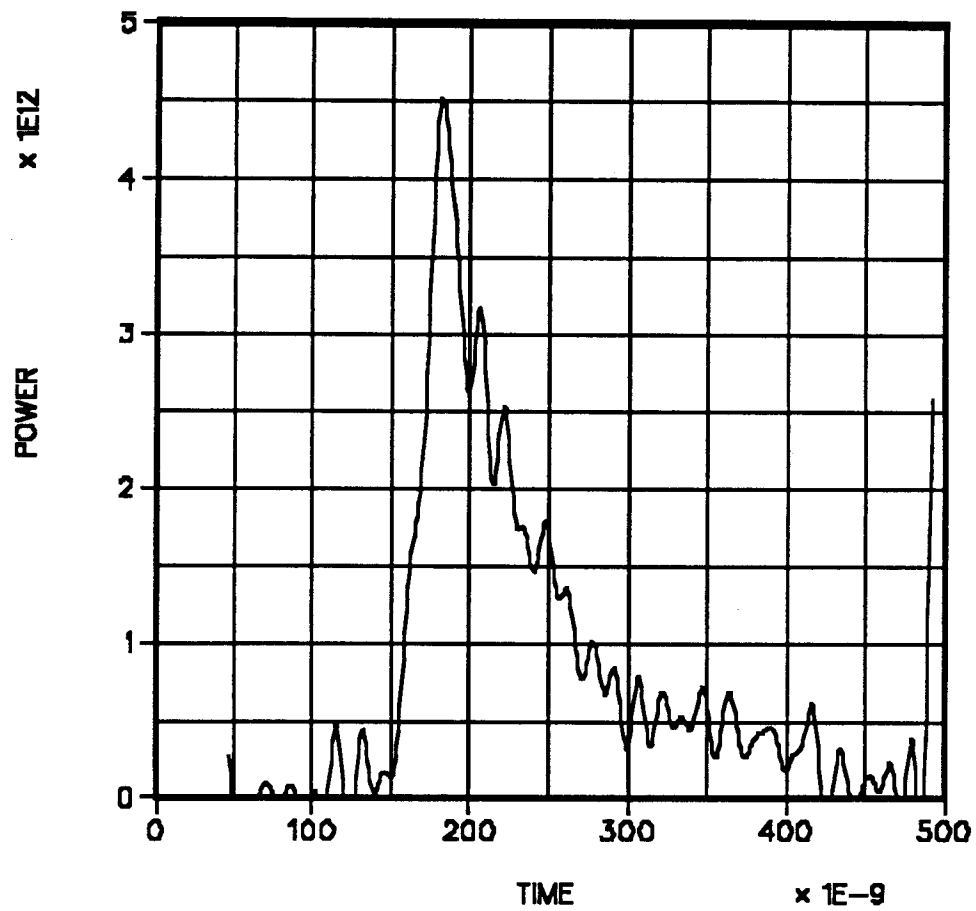


Figure 7.10. Total x-ray power versus time.

Table 7.4. Samples of Aluminum 6061 Irradiated with Argon Pinch X-rays on SATURN.

Sample #	Filtered	Coated	Time Delay (ns)
936A	No	No	600
936B	Yes	No	550
936C	No	Yes	580
936D	Yes	Yes	550

gage reaches its peak. There is probably an uncertainty of a few 10's of ns in the expected delay time because of the difficulty in choosing peaks. Also the shocks will be traveling faster than the speed of sound. The speed of the shock can increase by a factor of 2 over the range of shock pressures expected in the experiments, so one of the earlier pulses could be due to the shock. The latest experiments, which will not be reported here, have the gage signal recorded for a longer time so one can see the whole waveform. These measurements will also only show the pulse due to the shock striking the quartz gage. This will provide unambiguous data, which will be compared with simulations.

## 7.2. Microstructural Analysis of SATURN Samples

The microstructure of some aluminum 6061 samples shot on SATURN has been studied and compared with an unirradiated sample. The samples are given labels and described in Table 7.5. Of interest are changes in the microstructure induced by the vaporization and the passage of shocks through the unvaporized aluminum. The samples were first cut and polished, and then the microstructure was observed via optical microscopy, and measurements were made of the bulk hardness, the hardness as a function of position, and the composition of the surface was studied with electron microscopy. Less change was

Table 7.5. Samples of Aluminum 6061 Irradiated with X-rays on SATURN.

Sample #	Irradiated	Coating	Shot #
U	No	None	None
A1	Yes	Alumina	658
1	Yes	None	736
2	Yes	Graphite	736

observed in the material properties than expected and attempts are underway to try to understand these results.

### 7.2.1. Sample Preparation

Four samples of aluminum 6061-T6 were studied using optical metallography, scanning electron microscopy (SEM), microhardness and nanohardness testing. Samples were sectioned, mounted and polished to obtain a smooth scratch-free surface. Aluminum can be difficult to polish and alloy 6061-T6 was particularly difficult as it has large precipitates which tend to fall out during polishing. This causes pitting. Samples were mounted in Buehler Konductoment-1 mounting agent using a hot mount press. This agent was used because it is conductive and can be used in SEM with no charging problems. A second set of samples was mounted in epoxy. All samples were polished down with 600 grit emory paper. A second polishing was made with 1  $\mu\text{m}$  diamond paste. A final polish was applied with Buehler Mastermet colloidal 0.6  $\mu\text{m}$  silica polishing solution in a Buehler Minimet automatic polisher for 30 minutes. This method was used for the final polish because Buehler Mastermet is somewhat acidic and the automatic polisher allowed for no contact.

The slowest speed and lightest load were used to avoid the pitting problem. At this point, a final electropolish could have been used to remove any surface deformation. The most successful electropolishing technique found uses an electrolyte of 817 ml orthophosphoric acid, 134 ml sulfuric acid, 156 g chromic oxide and 40 ml water at 70°C and with a 10-12 V potential drop. However, electropolishing was not used because it was found that it preferentially removes the interface between the mount and the aluminum, making examination of cross-sectioned samples difficult.

### 7.2.2. Results

Photographs of the surfaces of the samples prior to being cut into cross-sections are shown in Fig. 7.11. Fig. 7.11a shows the machined surface of sample U, a disk of aluminum 6060-T6 which has not been irradiated. Sample A1, an irradiated piece that was originally coated with alumina, is shown in Fig. 7.11b. There is no longer any alumina present. Machining scratches are still present, indicating that very little of the aluminum substrate was vaporized. A photograph of the uncoated irradiated aluminum, sample 1, is shown in Fig. 7.11c. Sample 2, aluminum 6061-T6 coated with spray-on graphite, is shown in Fig. 7.11d. In samples 1 and 2 there are no traces of the original surface remaining. In sample 2, the holder protected the edge of the surface from the x-rays. Fortunately, parts of this edge-on sample 2 were not splashed with molten aluminum. In Fig. 7.12, this edge is shown in cross-section. One can see the raised lip on the edge of the sample. This shows that 120  $\mu\text{m}$  were removed from the surface by the x-rays.

A set of optical micrographs from the three irradiated samples, cut in cross-section, is shown in Fig. 7.13. The irradiated surface of sample A1 appears uneven, but few other changes in the microstructure of the surface are evident. One can clearly see a melt line in samples 1 and 2. The material to the right of the melt line has melted and resolidified, leaving a microstructure that is clearly different from the unmelted material. The melt line is flat across the whole surface of the sample, demonstrating the initial surface smoothness

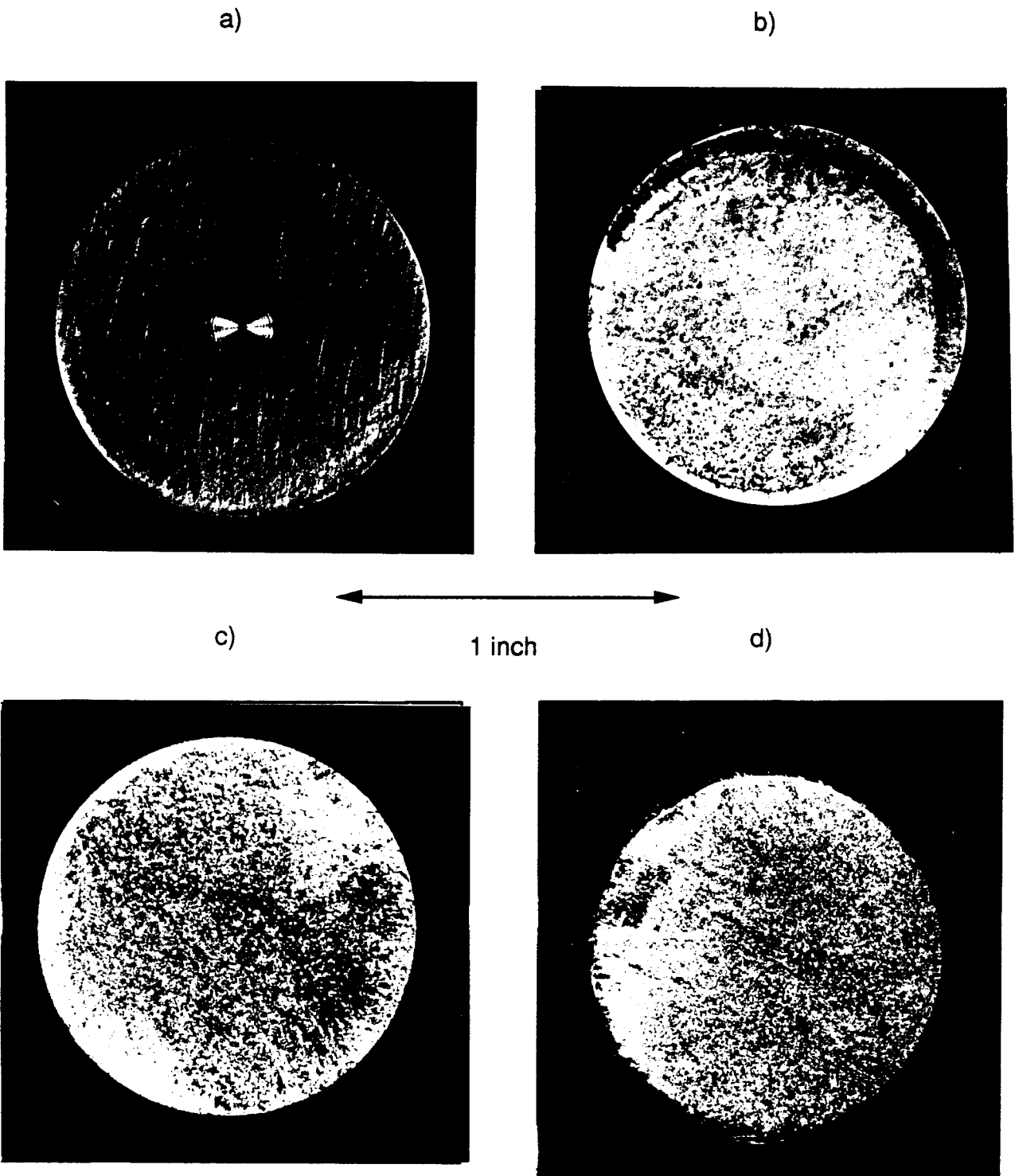


Figure 7.11. Photographs of the sample surfaces. a) Unirradiated, b) A1, c) 1, d) 2. The samples are 1 inch in diameter.

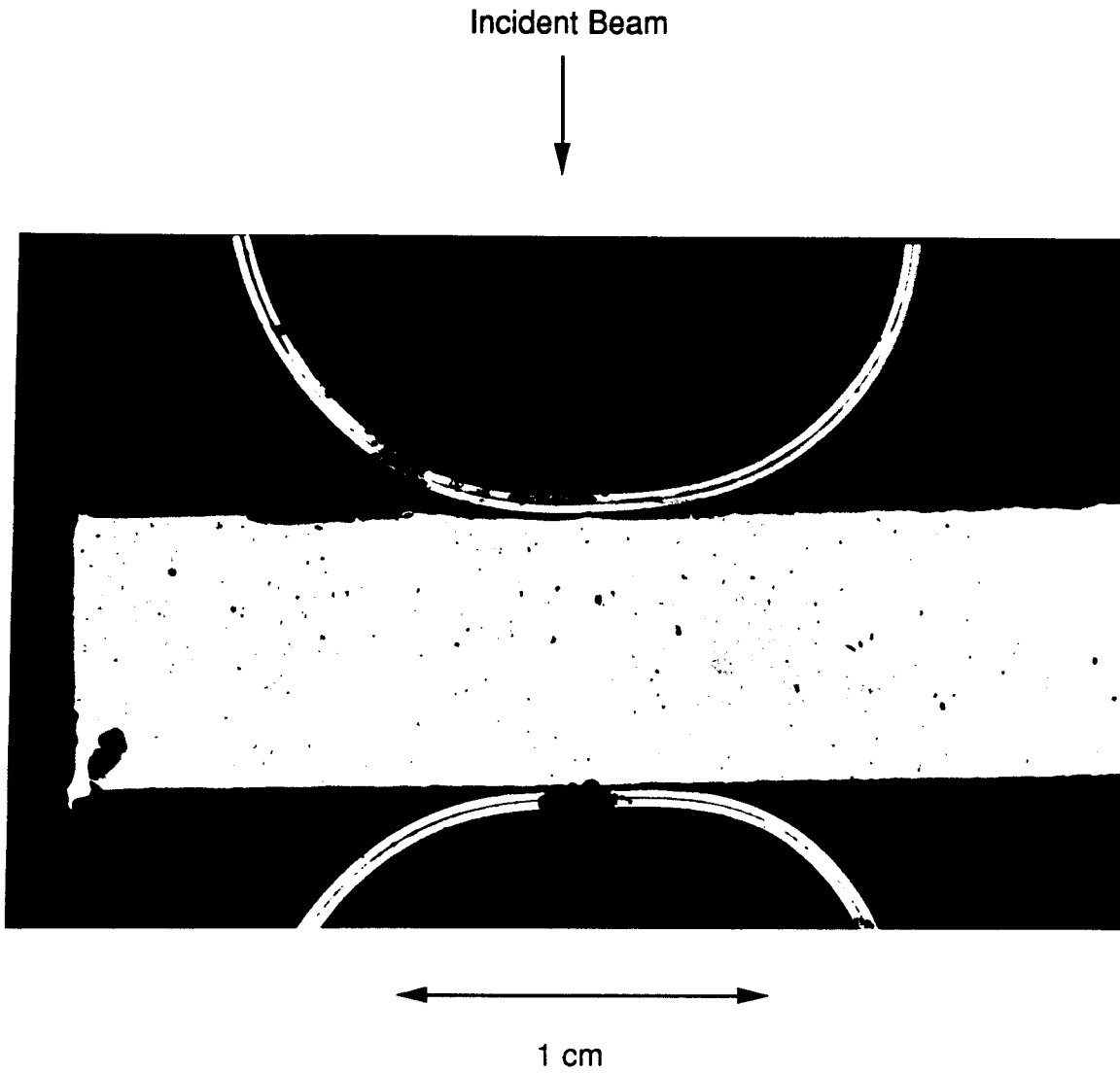


Figure 7.12. Photograph of Sample 2 in cross-section. The ledge on the left edge is due to unvaporized material. The x-rays were incident from the top.

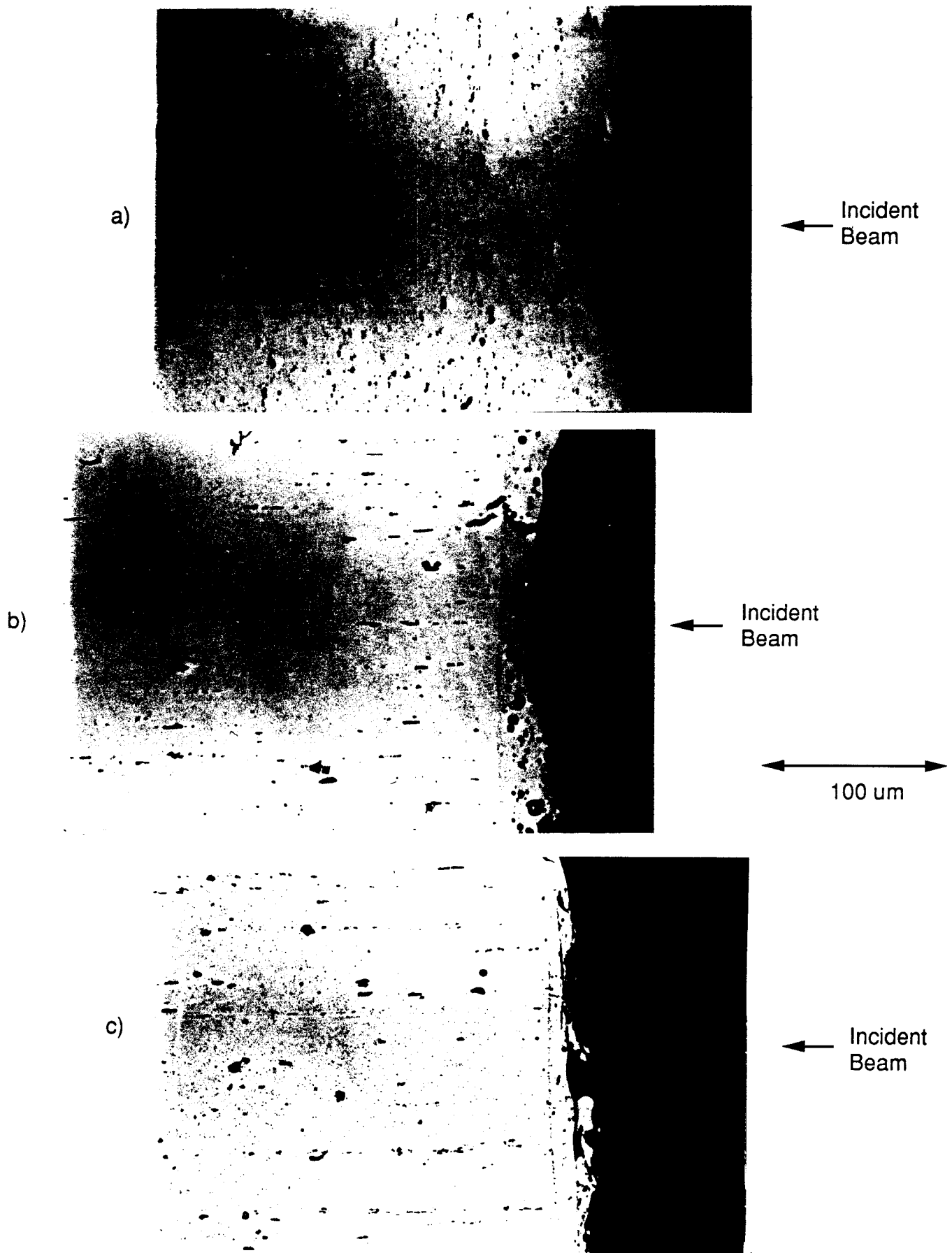


Figure 7.13. Optical micrographs showing irradiated samples cut in cross-section. a) A1, b) 1, c) 2.

Table 7.6. Bulk Microhardness Results from Samples Unirradiated and Irradiated with X-Rays on SATURN.

Sample #	Knoop Hardness #	Standard Deviation
U	113	11
A1	112	9
1	118	7
2	125	10

and the uniformity of the x-ray intensity. The surface is irregular because the material can splash while it is molten and because the surface is subjected to splatter from other sources in SATURN. The flat melt line implies that the shock generated in the material was very uniform, which is important in understanding the strain gage measurements discussed earlier.

Table 7.6 shows the microhardness measurements taken from the four samples. Microhardness was measured within the bulk of all samples, away from the vaporized surfaces. A load of 50 g and a Knoop indenter were used in these measurements. The results show little change in the microhardness from sample to sample. This seems to indicate that the passage of shocks has no effect on the microhardness.

Microprobe measurements on the samples were also completed. Hardness versus depth into the material is shown in Fig. 7.14, with the irradiated surface being zero depth. More scatter is observed in the data near the sample surfaces because, even though electropolishing was not used, some relief of the surface/mount interface occurred during mechanical polishing. The hardness profiles of all samples were rather flat away from the surface. One can see a drop in the hardness just beyond the melt line in samples 1 and 2. This may either be due to sub-melt heating of the material or to the passage of strong shocks through

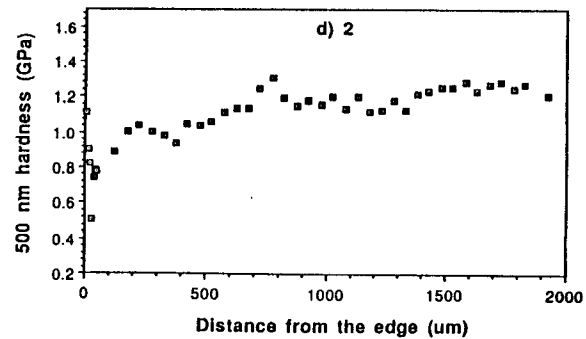
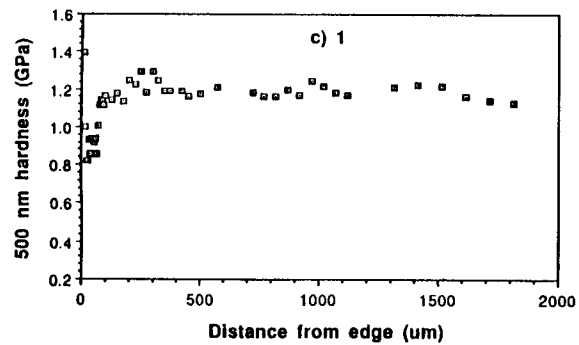
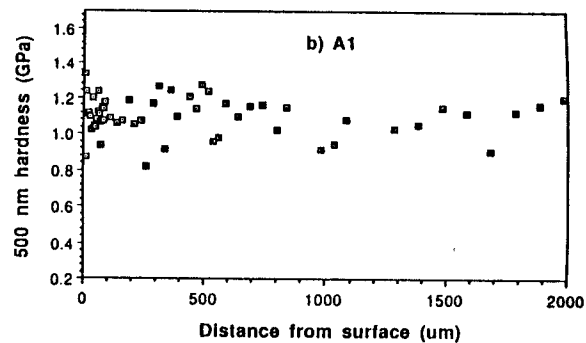
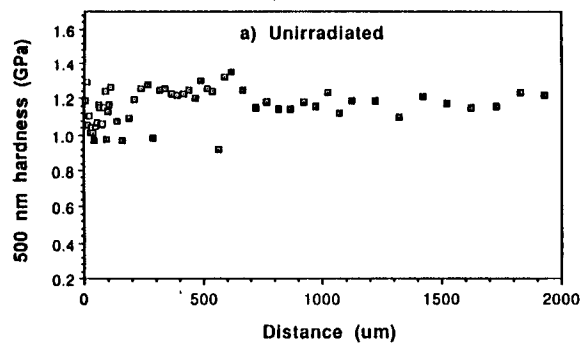


Figure 7.14. Hardness versus depth into sample: a) unirradiated, b) A1, c) 1, d) 2.

this region. Within the melt region of these two samples, one sees the hardness increase again. In all four samples, the nanohardness in the center of the material is 1.2 GPa. The lack of change in the bulk properties is in agreement with the microhardness results.

In an attempt to understand the nature of the melted layer, an SEM image of the cross-sectioned sample 2 was taken, and is shown in Fig. 7.15. The image is created with back-scattered electrons, so the contrast is due to changes in the composition of the material. The bright layer is iron rich material. In Figs. 7.16 and 7.17, the energy dispersive spectra (EDS) of x-rays emitted from sample 2 under the SEM electron beam are shown. Figure 7.16 shows the spectrum from the center of the sample and clearly shows the aluminum peak. Fig. 7.17 shows the spectrum from the surface, that is, the bright region in Fig. 7.15. One can clearly see the contributions of iron, chromium, nickel, and silicon, in addition to aluminum. Therefore, the melted material in sample 2 is at least partially due to material splattered onto the surface from elsewhere in SATURN. Elsewhere could include from the sample holder, which was made of steel. These features were also seen on other samples. The amounts of these materials were very nonuniform across the surface of the samples.

## 8. Fill Gas Heating by Ion Beams

The properties of a target chamber fill gas for the LMF have been studied. Specifically, it is desirable to calculate the electrical conductivity of the 1 torr helium gas through which driver ions are ballistically focussed. A high electrical conductivity is important to the propagation of the ion beam. A conductivity greater than approximately  $10^{14} \text{ s}^{-1}$  is thought to avoid the filamentation instability. The SCATBALL computer code was developed to calculate the heating of the fill gas due to the beam. Then the electrical conductivity was calculated at the tail of the ion beam for the LMF base case parameters. It was found that the required conductivity can be obtained.

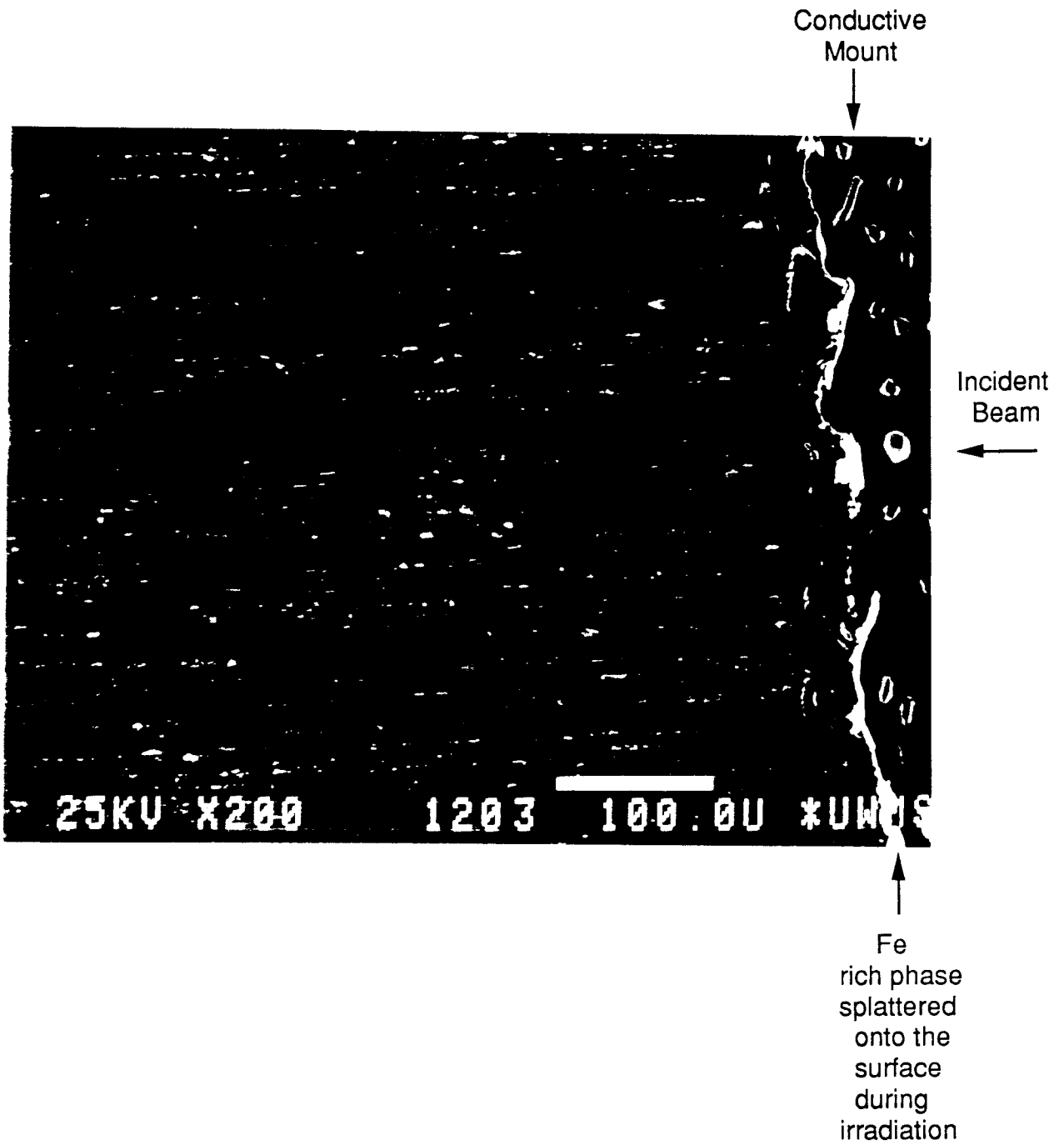


Figure 7.15. SEM micrograph of Sample 2 showing the presence of another material in the melt layer.

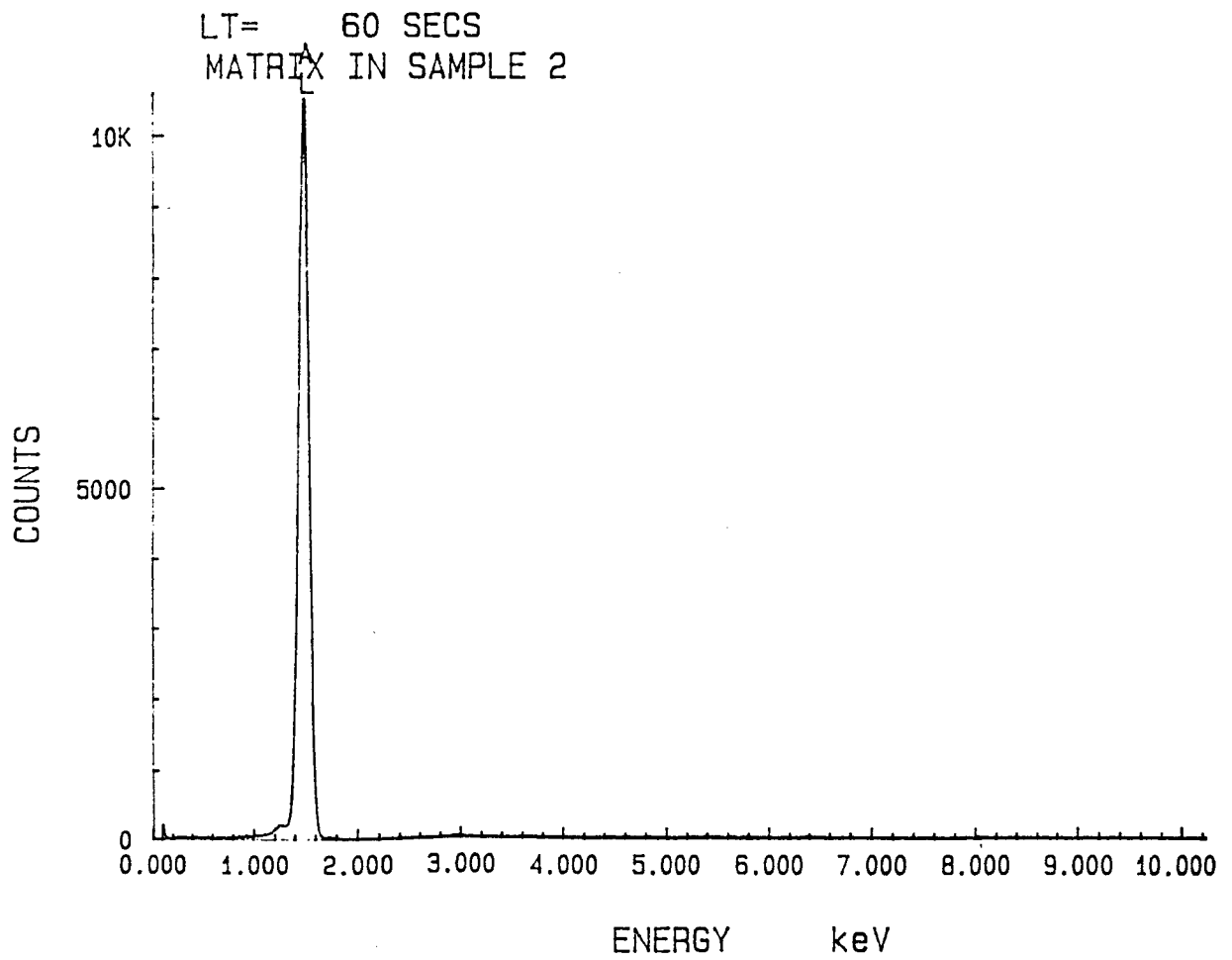


Figure 7.16. EDS spectrum from the bulk of Sample 2.

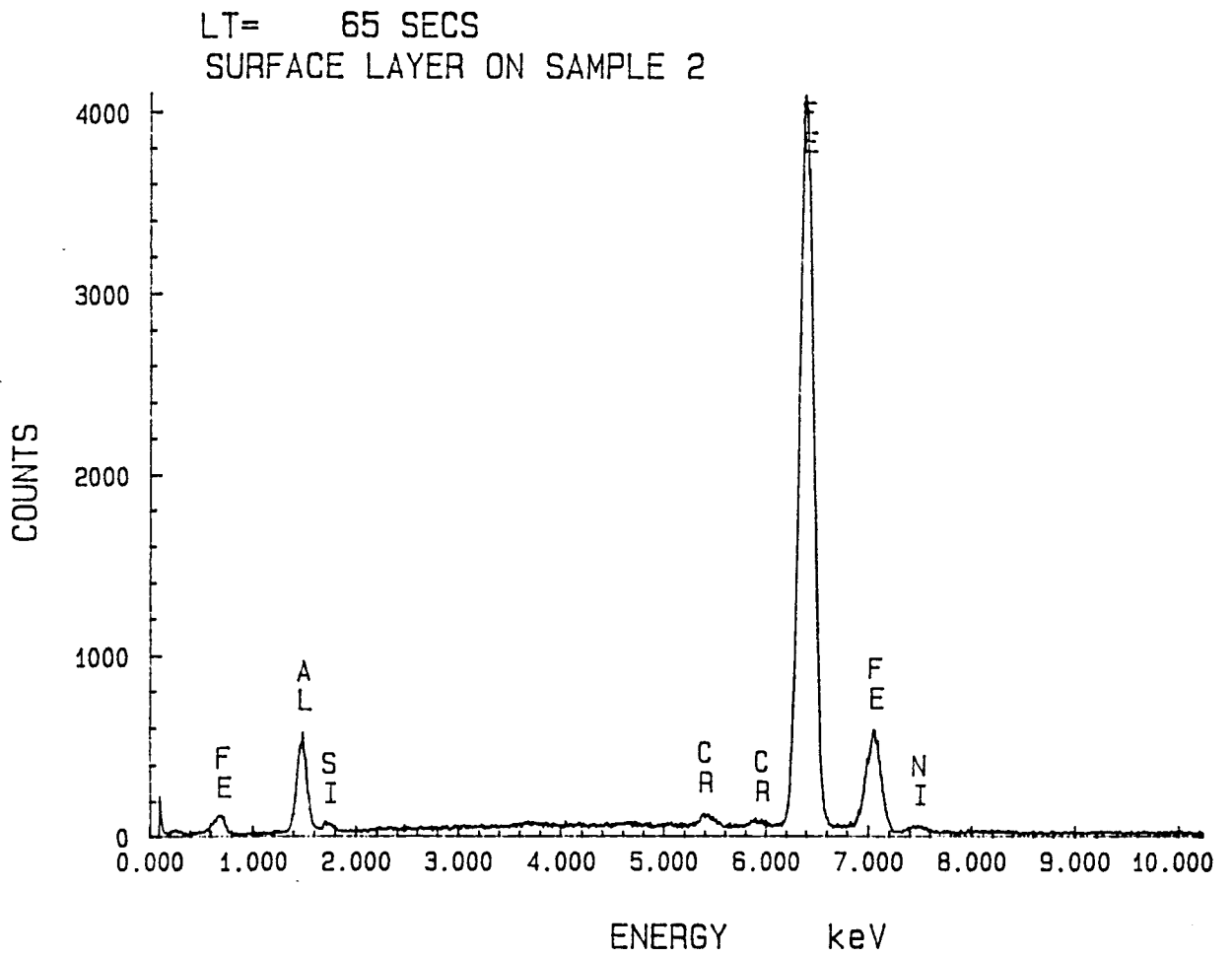


Figure 7.17. EDS spectrum from the surface of Sample 2.

### 8.1. The SCATBALL Computer Code

SCATBALL calculates the width of the beam envelope as it moves through the drift and focus regions. It includes the effects of microdivergence, scattering, and geometrical focusing. Included in the scattering are the effects of a foil, if one is present. SCATBALL uses the formalism developed by Craig Olson of SNL for the beam envelope. This provides the beam area as a function of distance from the diode. Given the energy per ion, the current density on the anode surface, and the time-of-flight bunching of the ion beam, one completely prescribes the beam current density and power intensity at any point in the transport. With this, the ohmic heating of the gas by the current can be calculated. It was assumed that the beam is fully current neutralized, so the electron return current density is equal to the ion beam current density. Therefore, the ohmic heating rate per unit volume is

$$P_{ohmic} = \rho \times j_o \times (A_{beam}(x)/A_{anode}) \times (\tau_{anode}/\tau(x)), \quad (11)$$

where  $j_o$  is the current density on the anode,  $A_{beam}(x)$  is the beam area,  $A_{anode}$  and  $\tau_{anode}$  are the area and pulse width of the anode and  $\tau(x)$  is the pulse width of the beam.  $\tau$  is a function of position because of time-of-flight bunching, which is assumed to linearly compress the pulse.  $\rho$  is the resistivity of the gas, which is a function of temperature. The temperature of the gas is calculated from the energy per unit mass using the Saha model for ionization. In addition to the temperature at a given energy density, the code calculates the charge state of the gas. The conductivity (the inverse of  $\rho$ ) is

$$\sigma = N_{gas} Z e^2 / m_e \nu \quad (12)$$

where the collision frequency is

$$\nu = \nu_{electron-ion} + \nu_{electron-neutral} \quad (13)$$

$$\nu_{electron-ion} = 8.608 \times 10^{-7} N_{gas} Z^2 \ln \Lambda T^{3/2} (1 + Z) / Z \quad (\text{s}^{-1}) \quad (14)$$

$$\nu_{electron-neutral} = 6 \times 10^{-16} N_{neutral} \sqrt{kT/m_e} \quad (\text{s}^{-1}). \quad (15)$$

Here,  $T$  is the electron temperature in eV and  $Z$  is the charge state of the gas.  $N_{gas}$  and  $N_{neutral}$  are number densities.  $(Z+1)/Z$  in Eqn. 14 is to account for electron-electron collisions [?].  $\nu_{electron-neutral}$  is only valid for helium. An alternative expression for the electron-ion collision frequency used in similar calculations by Swegle and Slutz [?] is

$$\nu_{electron-ion} = 1.45 \times 10^{-6} N_{gas} Z^2 \ln \Lambda T^{3/2} \quad (\text{s}^{-1}). \quad (16)$$

Both forms of the electron-ion collision frequency have been used and will show some minor differences in the results. Conductivities calculated using Eqn. 14 are referred to as the derived conductivity. The conductivities calculated with Eqn. 16 will be called the Swegle and Slutz conductivity. In addition to the ohmic heating, the direct heating by the ion beam has been included using the model developed by Mehlhorn [?] and modified for the CONRAD code [?].

The equations to be solved by SCATBALL are nonlinear in temperature. This has been approached by calculating the heating of the gas as a function of time with many time steps. Additionally, each time step has internal iterations.

## 8.2. LMF Results

SCATBALL code calculations for the light ion LMF have been carried out. The parameters used in these calculations are shown in Table 8.1. The nature of the gas response as a function of time is shown in Figs. 8.1 and 8.2, for the behavior at the entrance to the target chamber and at the target, respectively. One notices that the conditions at the chamber entrance do not change much from the initial conditions, where the energy density was set to 0.1 J/cm<sup>3</sup>. At the target, the conditions do change drastically. The temperature gets unrealistically high because SCATBALL includes no radiation losses, which would not allow the temperature to get up to hundreds of eV.

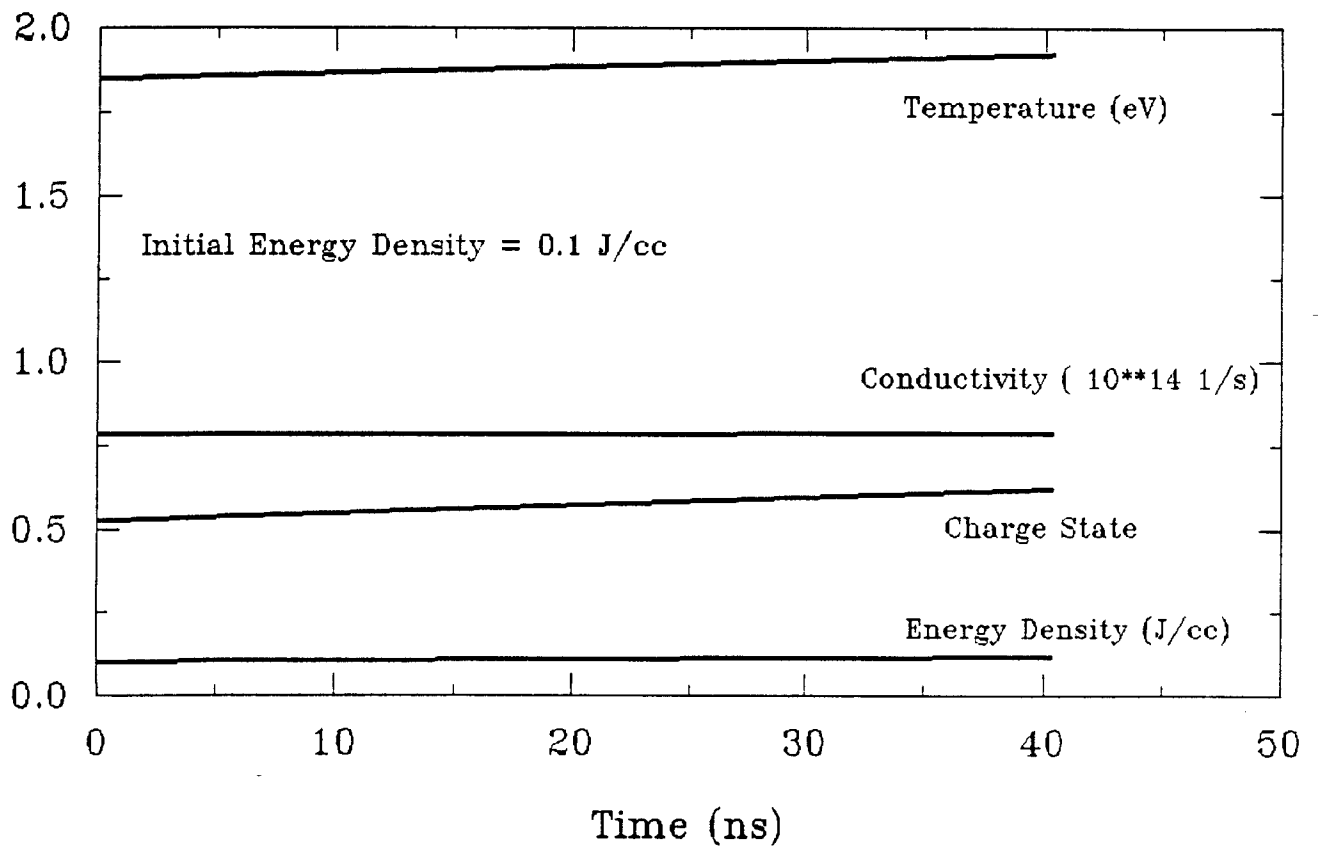


Figure 8.1. Fill gas response at chamber entrance.

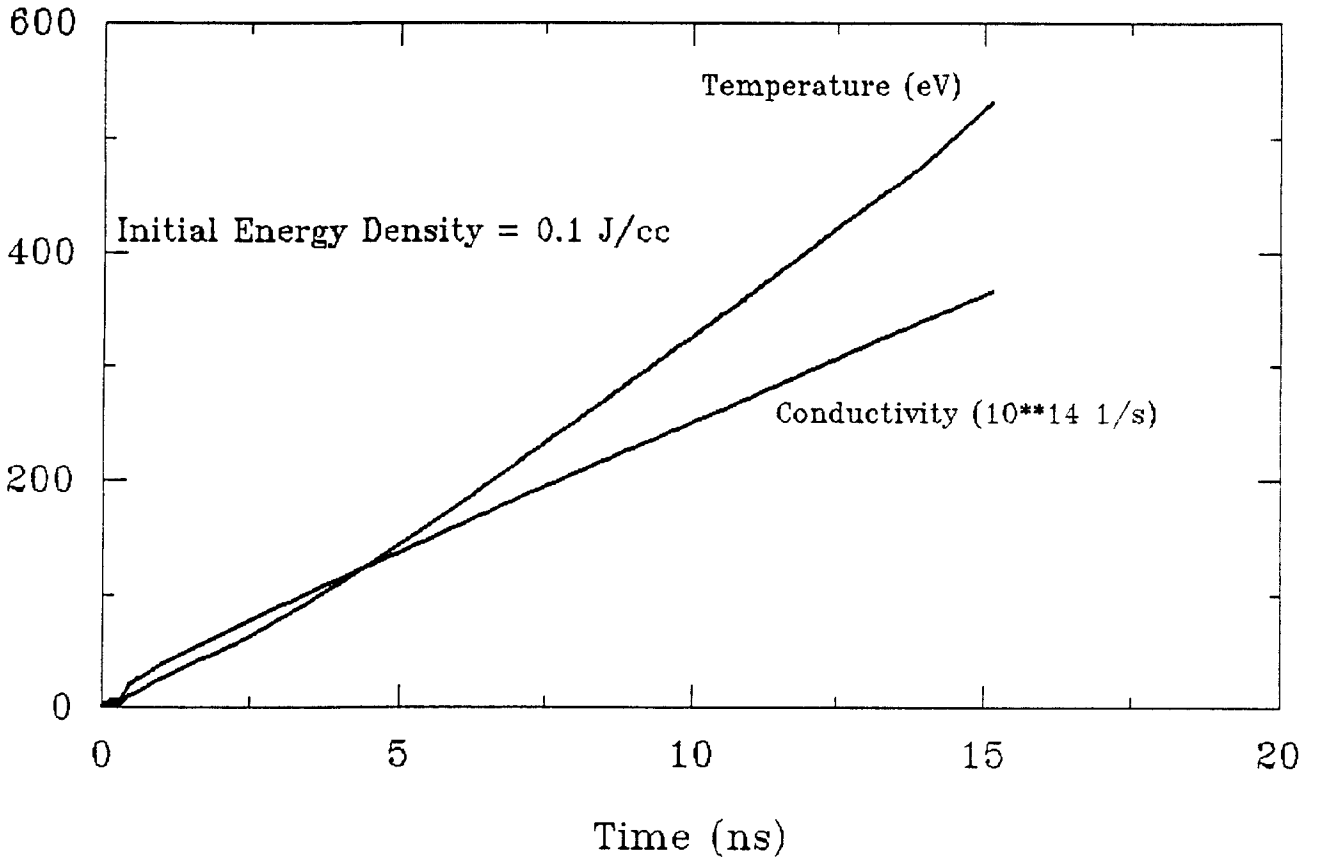


Figure 8.2. Fill gas response at target.

Table 8.1. Beam Transport Parameters for Light Ion LMF.

Anode area	600 cm <sup>2</sup>
Focal length	150 cm
Drift length	250 cm
Fill gas	Helium
Gas density	1 torr
Beam ion energy	30 MeV
Diode pulse width	40 ns
Microdivergence	6 mrad
Anode current density	2 kA/cm <sup>2</sup>
Anode power density	.06 TW/cm <sup>2</sup>
Power per anode	36 TW
Energy per anode	1.44 MJ
Ions per pulse	$3.0 \times 10^{17}$
Beam density	$4.35 \times 10^{12}$ cm <sup>-3</sup>
Z for neutralization	$1.23 \times 10^{-4}$

Studies were made of the sensitivity of the condition of the fill gas at the entrance of the target chamber at the tail of the ion beam to the initial energy density. The initial energy density in the gas could be due to avalanche heating, driven by transient fields at the head of the beam, or to some form of applied heating. Results are shown for the LMF in Figs. 8.3 and 8.4, where the final energy density, the average charge state, the plasma temperature and the conductivity are plotted against the initial energy density. This was done for the derived conductivity and for the Sweigle and Slutz conductivity. In both cases, one sees that the energy density increases approximately linearly with initial energy density, but that the temperature has a step-like form. This is because the equation of state is non-ideal, due to the heating of ionizing the gas, as is shown in Fig. 8.5. In the derived conductivity calculations, the conductivity is monotonically increasing with initial energy density and becomes greater than  $1 \times 10^{14}$  s<sup>-1</sup> at about 0.15 J/cm<sup>3</sup> initial energy density. The Sweigle and Slutz calculations show the conductivity following a more complicated form, but the conductivity is always above  $1 \times 10^{14}$  s<sup>-1</sup>.

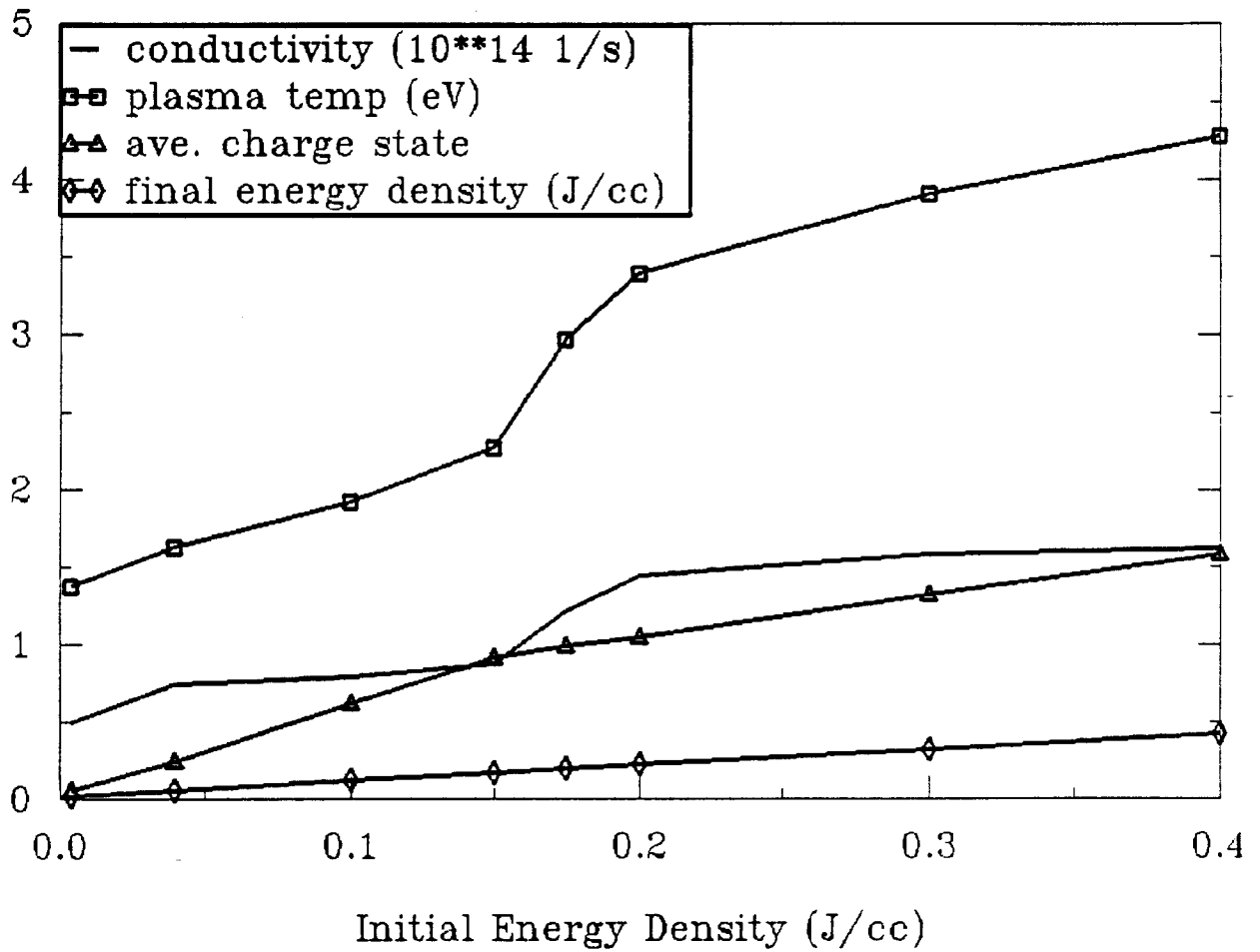


Figure 8.3. Fill gas response at chamber entrance versus initial energy density. The derived conductivity model was used.

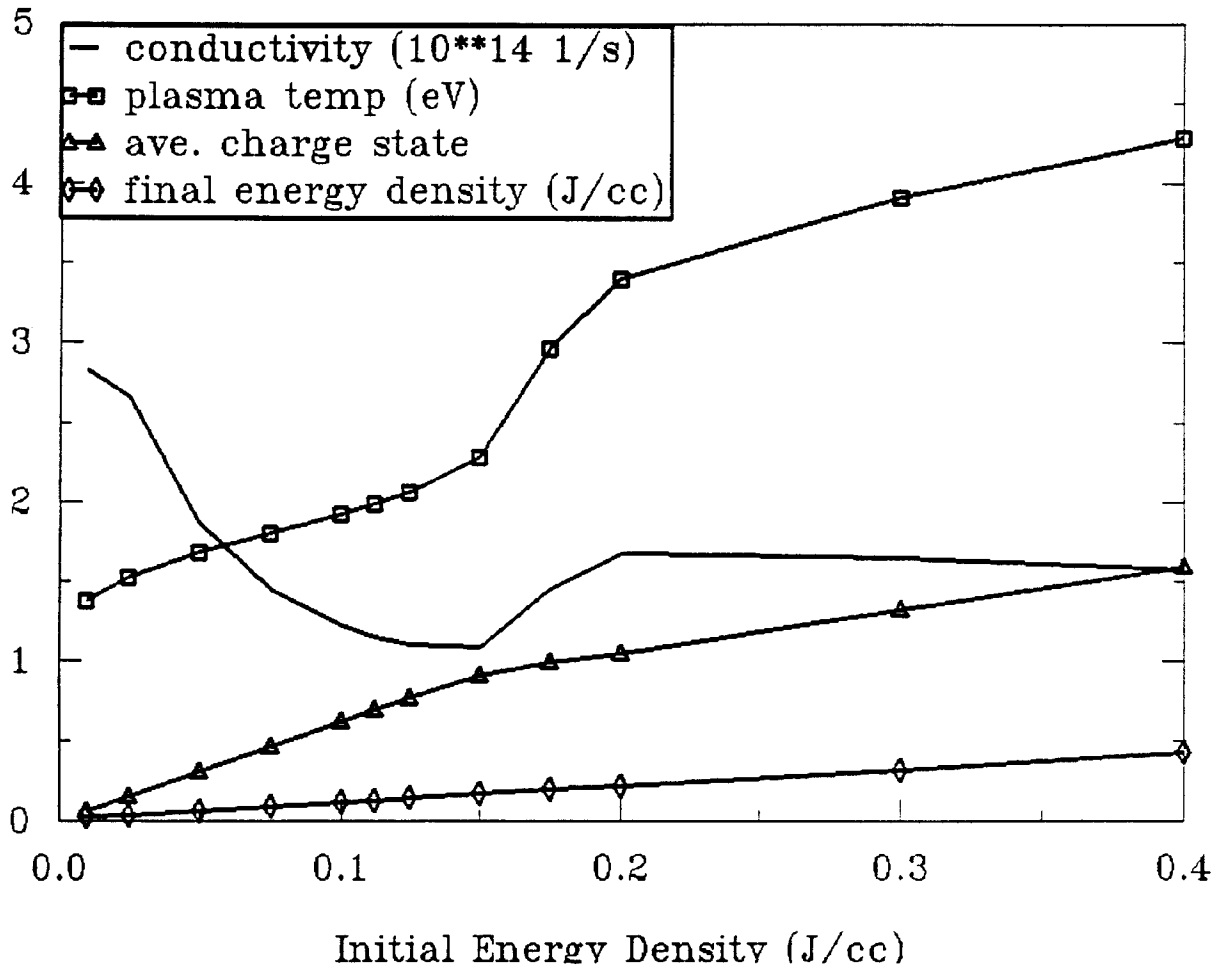


Figure 8.4. Fill gas response at chamber entrance versus initial energy density. The Swegle and Slutz conductivity model was used.

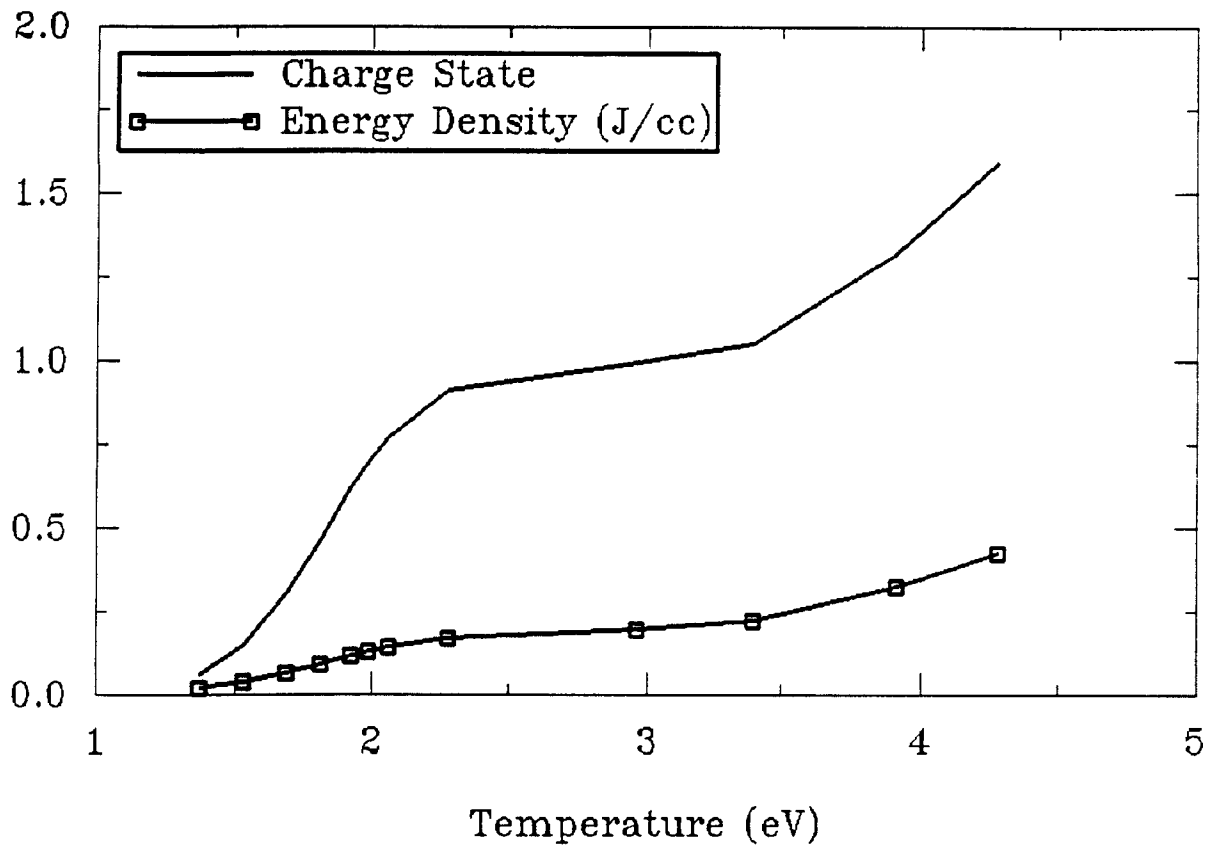


Figure 8.5. Equation of state for helium.

Studies were also made of the spatial form of the gas properties at the tail of the beam. These calculations were done for an initial energy density of  $0.1 \text{ J/cm}^3$  and for both conductivity models. Figures 8.6 and 8.7 show the energy density, temperature, charge state, and conductivity versus position for the derived conductivity model. The same is shown for the Swegle and Slutz conductivity in Figs. 8.8 and 8.9. In both cases, the conductivity is plotted as  $\log(\text{conductivity (s}^{-1}\text{)}) - 14$ , so zero is equivalent to  $1 \times 10^{14} \text{ s}^{-1}$ . For both models, the conductivity is close to or above  $1 \times 10^{14} \text{ s}^{-1}$ . Near the target, one sees that as the gas heats and becomes fully stripped, the temperature and conductivity rapidly increase as one moves closer to the target. This occurs because no more energy is taken by ionization and because the collision frequency is roughly proportional to  $Z^2/T^{3/2}$ . Once the gas is fully ionized,  $Z$  remains constant while  $T$  increases.

## 9. Conclusions

More than two years have been spent studying a number of issues related to the design of the light ion LMF. Four general areas of concern have been studied as prescribed in our contractual statements of work:

1. Analysis of the LMF target chamber.
2. Experiments on the response of first wall materials to intense x-rays.
3. Analysis of bulk structural response of the LMF target chamber.
4. Analysis of behavior of the fill gas in the LMF target chamber during heating by the driver ion beam.

In addition, contributions to the LMF effort have been made as it seemed appropriate. This included considerations of target cooling and support (Chapter 5) and participation in the writing of joint reports and participation in the presentations to various committees reviewing the national ICF program.

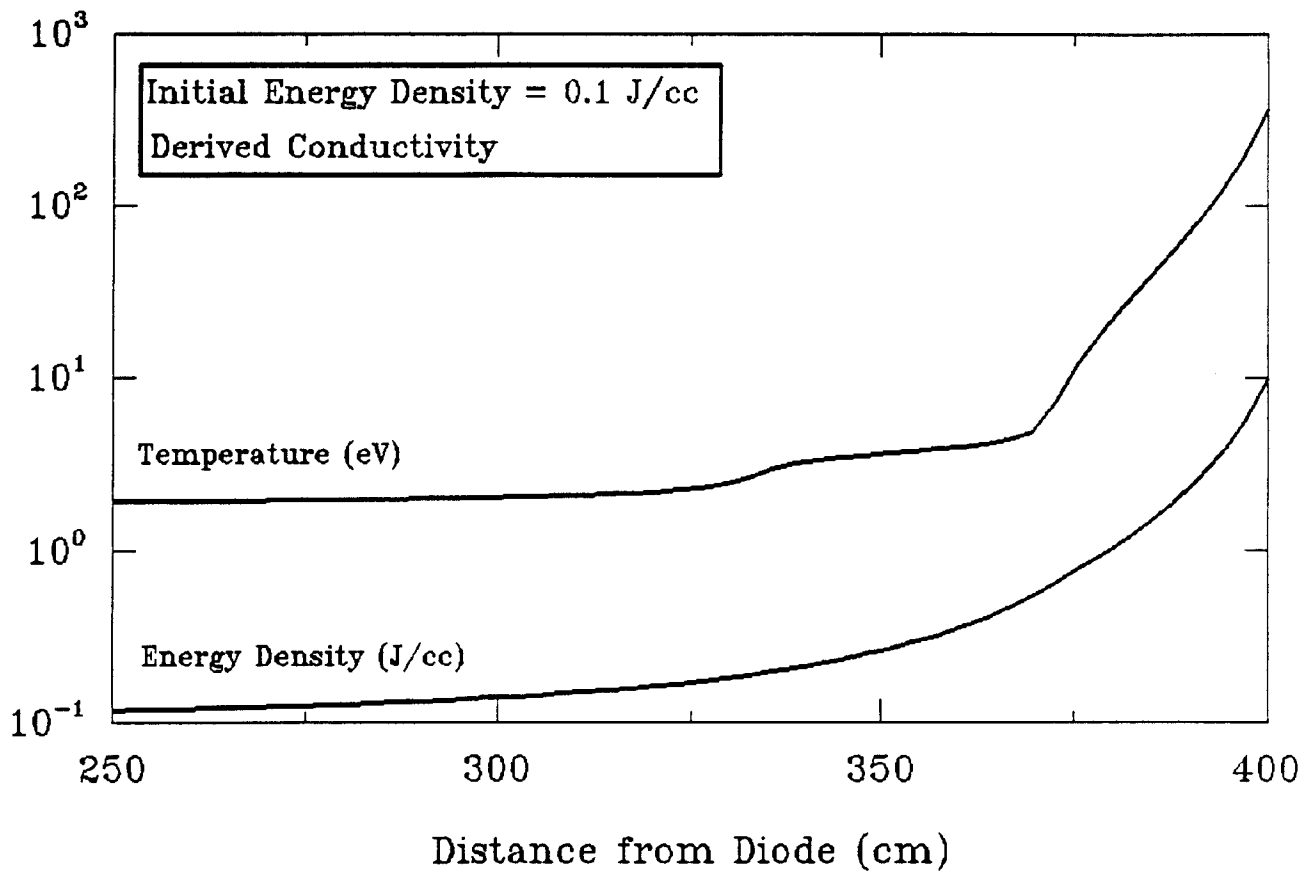


Figure 8.6. Energy density and temperature in fill gas versus position. The derived conductivity is used.

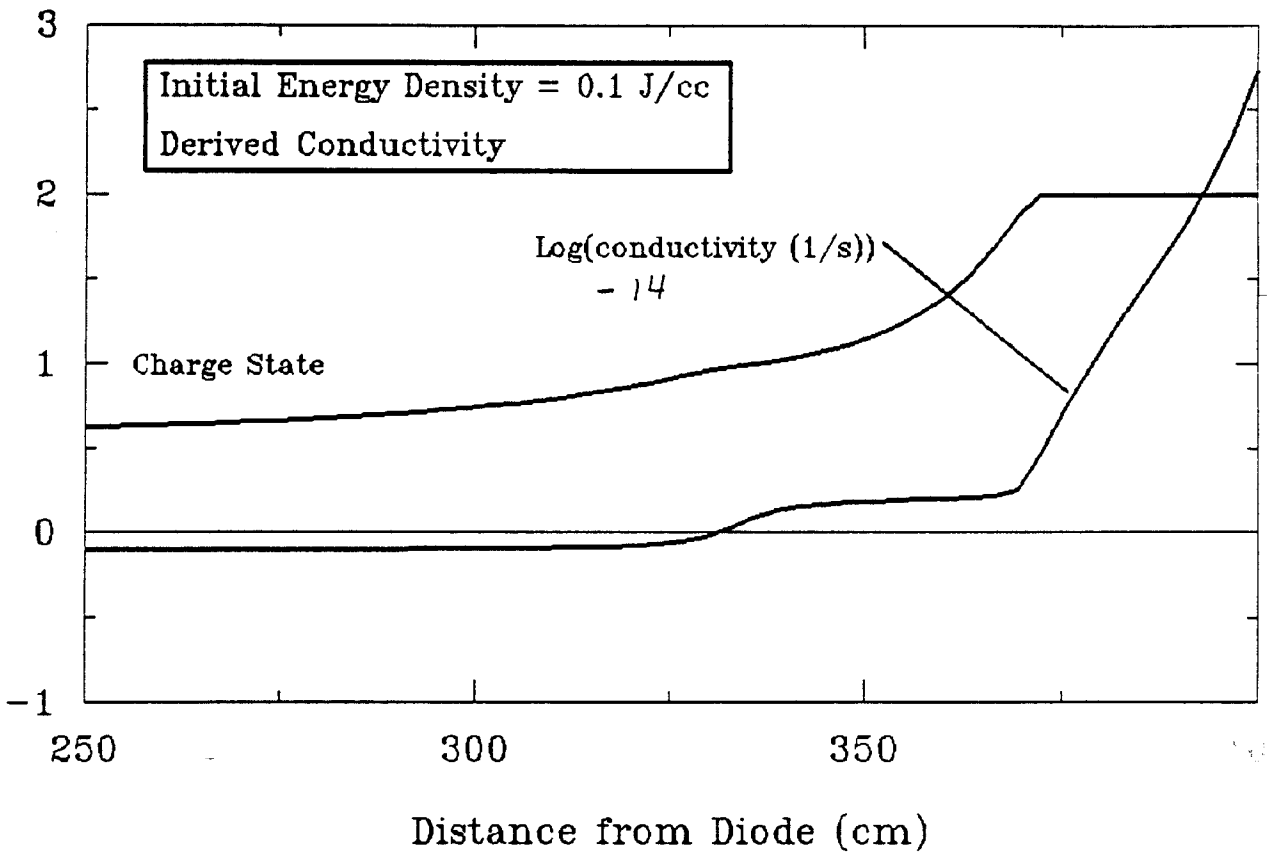


Figure 8.7. Charge state and conductivity in fill gas versus position. The derived conductivity is used.

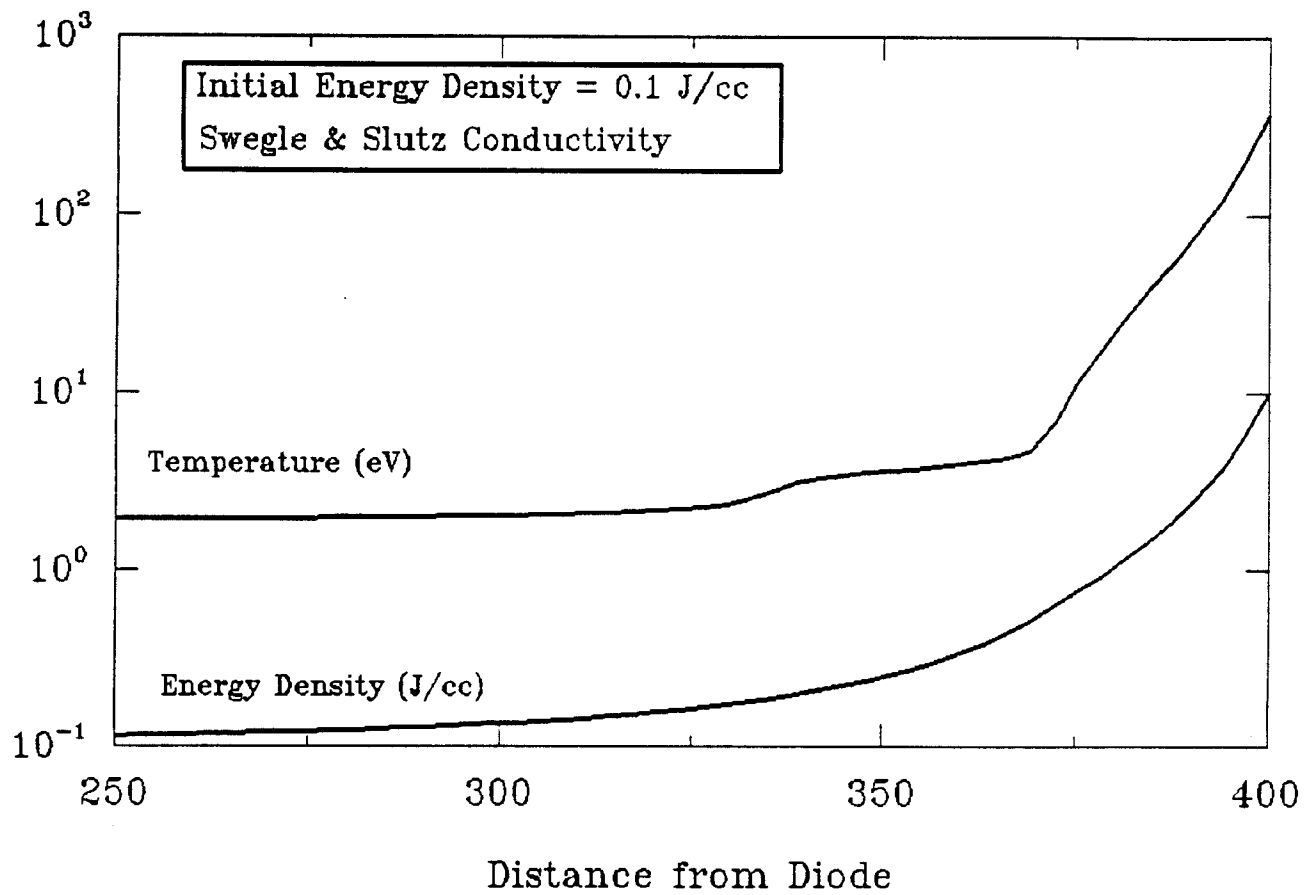


Figure 8.8. Energy density and temperature in fill gas versus position. The Swegle and Slutz conductivity is used.

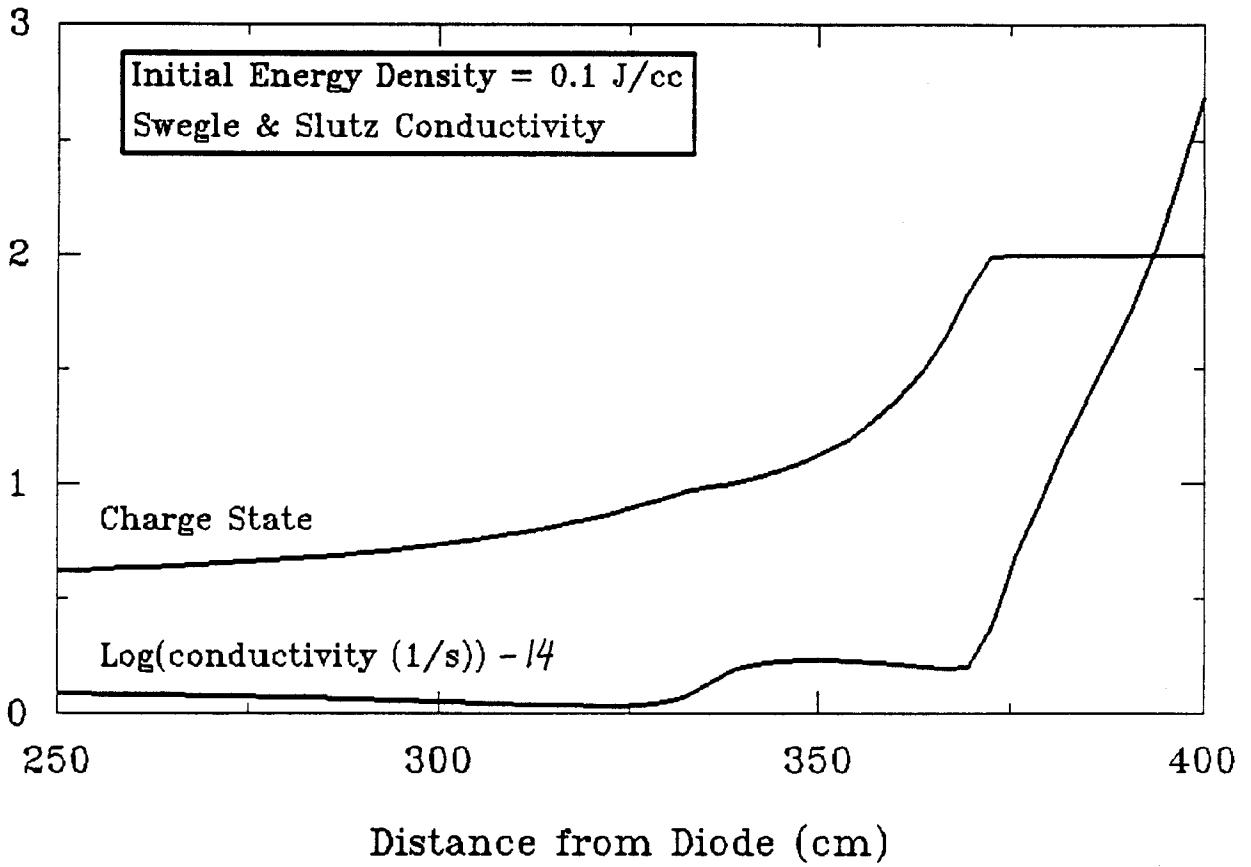


Figure 8.9. Charge state and conductivity in fill gas versus position. The Swegle and Slutz conductivity is used.

The LMF effort is on-going at the national labs including SNL. The effort at UW is by no means complete. Although there has been good interaction on the design with scientists at SNL who are responsible for other parts of the facility, there are still inconsistencies that need resolution. For example, in simulation experiments, the target chamber is likely to be lined with LiH to reflect the soft x-rays. The x-rays will, therefore, not vaporize wall material on the simulation shots. Some other issues involve on-going work, such as the consideration of the structural response of the beam transport tubes in the three meter radius design. It is also believed that the facility design could be better optimized to allow lower overall costs, which would change some target chamber parameters.

It is believed that the most significant accomplishments have been in developing computer and analytic methods, and a technology base required for a credible LMF design. The designs will undoubtedly evolve further before an LMF is built. So the various designs, which have been designed and analyzed for more than two years, will probably undergo major changes. These changes will result from better information on materials, beam propagation, target performance, and diode performance that will be provided by experiments on PBFA-II, SABRE, NOVA-Upgrade, and SATURN. Other programs, for example in magnetic fusion energy and the aerospace industry, will also be good sources of information, especially in the area of materials. The requirements on LMF performance are also evolving, which will lead to design changes. By keeping analytical tools up to date, and by working on the basic technologies required for the LMF, it will be possible to address the changes in the LMF and design the optimum LMF target chamber.

In summary, it is felt that significant contributions have been made to the progress of LMF target chamber design and analysis, but that many issues remain.

## Acknowledgements

Many people at SNL deserve acknowledgement for help in performing this work. One of us (RRP) spent 9 months at SNL during the contract period and is very thankful for the hospitality of many people. He would like to particularly thank Ken Prestwich, Craig Olson, Rick Olson, Rick Spielman, Juan Ramirez, and Don Cook. Rick Spielman and his technicians also helped us a great deal in the SATURN experiments. Dennis Croessmann has graciously provided samples to irradiate on SATURN. Some samples were also supplied by Dennis Slaughter of Lawrence Livermore National Laboratory.

Many of the computer calculations presented here were performed on San Diego Supercomputer Center computers.

Funding was provided by the U.S. Department of Energy.

The help of Dennis Bruggink in assembling this report is also appreciated.

## References

- [1] R.R. Peterson, et al., “An Overview of the Target Chamber Design and Analysis for the Light Ion Beam Laboratory Microfusion Facility,” University of Wisconsin Fusion Technology Institute Report UWFD-819 (February 1990).
- [2] R.O. Bangerter, “Targets for Heavy Ion Fusion,” *Fusion Tech.* 13, 348 (1988).
- [3] B. Badger, et al., “LIBRA - A Light Ion Beam Fusion Conceptual Reactor Design,” University of Wisconsin Fusion Technology Institute Report UWFD-800 (February 1990).
- [4] R.R. Peterson, J.J. MacFarlane, and G.A. Moses, “CONRAD - A Combined Hydrodynamic-Condensation/Vaporization Computer Code,” University of Wisconsin Fusion Technology Institute Report UWFD-670 (July 1988).
- [5] R.R. Peterson, “Pressure Loadings on the Walls of a Light Ion Laboratory Microfusion Facility Target Chamber,” *Fusion Tech.* 19, 669 (1991).
- [6] R.R. Peterson, “Investigations into X-Ray Damage to the First Wall of the Inertial Confinement Fusion Laboratory Microfusion Facility,” Proceedings of the Ninth International Workshop on Laser Interaction and Related Plasma Phenomena, 6-10 November 1989, Monterey, CA.
- [7] R.L. Engelstad, J.W. Powers, and E.G. Lovell, “Mechanical Design of the LMF Target Chamber,” *Fusion Tech.* 19, 697 (1991).
- [8] Laser Program Annual Report 1983, Lawrence Livermore National Laboratory Report UCRL-50021-83 (1984), ed. C.D. Hendricks.
- [9] Laser Program Annual Report 1987, Lawrence Livermore National Laboratory Report UCRL-50021-87 (1989), ed. L.W. Coleman.

- [10] Laser Program Annual Report 1984, Lawrence Livermore National Laboratory Report UCRL-50021-84 (1985), ed. E. Storm.
- [11] R. O'Dell, et al., "User's Manual for ONEDANT: A Code Package for One-Dimensional, Diffusion-Accelerated, Neutral Particle Transport," LA-9184-M, Los Alamos National Laboratory, 1982.
- [12] M.E. Sawan, et al., "Nuclear Analysis of the Heavy-Ion-Beam-Driven Fusion Reactor HIBALL," Nuclear Technology/Fusion, Vol. 4, pp. 79-92, July 1983.
- [13] D.L. Henderson and O. Yasar, "DKR-ICF: A Radioactivity and Dose Rate Calculation Code Package," Vol. 1, University of Wisconsin Fusion Technology Institute Report UWFD-714 (April 1987).
- [14] D.L. Henderson, A.M. White, and G.A. Moses, "Target Material Activation Calculations for High Gain Light Ion Fusion Targets," University of Wisconsin Fusion Technology Institute Report UWFD-572 (April 1984).
- [15] W. Engles, "A User's Manual for ANISN," RSIC Code Package CCC-254, Radiation Shielding and Information Center, Oak Ridge National Laboratory, Oak Ridge, TN.
- [16] D.E. Grady, "Local Inertial Effects in Dynamic Fragmentation," J. Appl. Phys. 53, 322 (1982).
- [17] T. Endo, H. Shiraga, K. Shihoyama, and Y. Kato, "Generation of a Shock Wave by Soft - X-Ray - Driven Ablation," Phys. Rev. Lett. 60, 1022 (1988).
- [18] J.D. Jackson, "Classical Electrodynamics," John Wiley & Sons, Inc., New York, 1962.
- [19] J.A. Swegle and S.A. Slutz, J. Appl. Phys. 60, 10 (1986).
- [20] T.A. Mehlhorn, "Finite Material Temperature Model for Ion Energy Deposition in Ion-Driven ICF Targets," Sandia National Laboratory Report SAND80-0038 (May 1980).